Magnetic resonance imaging on sodium nuclei. Potential medical applications of ^{23}Na MRI

E.G. Sadykhov[1], Yu.A. Pirogov[2], N.V. Anisimov[2], M.V. Gulyaev[2], G.E. Pavlovskaya[3,4], T. Meersmann[3,4], V.N. Belyaev[1], D.V. Fomina[2]

[1]*National Research Nuclear University "MEPhI", Moscow, Russia*

[2]*Lomonosov Moscow State University, Moscow, Russia*

[3]*Sir Peter Mansfield Imaging Centre, School of Medicine, University of Nottingham, NG7 2RD, United Kingdom*

[4]*NIHR Nottingham Biomedical Centre, NG7 2RD, United Kingdom*

Yu.A. Pirogov, e-mail: yupi937@gmail.com

N.V. Anisimov, e-mail: anisimovnv@mail.ru

M.V. Gulyaev, e-mail: mihon-epsilon@yandex.ru

G.E. Pavlovskaya, e-mail: Galina.Pavlovskaya@nottingham.ac.uk

T. Meersmann, e-mail: Thomas.Meersmann@nottingham.ac.uk

V.N. Belyaev, e-mail: VNBelyaev@mephi.ru

D.V. Fomina, e-mail: dv.fomina@physics.msu.ru

Corresponding author: E.G. Sadykhov; e-mail: forward1292@gmail.com; ORCID: 0000-0001-8612-4765

Abstract

Sodium is a key element in a living organism. The increase of its concentration is an indicator of many pathological conditions. ^{23}Na MRI is a quantitative method that allows to determine the sodium content in tissues and organs *in vivo*. This method has not yet entered clinical practice widely, but it has already been used as a clinical research tool to investigate diseases such as brain tumors, breast cancer, stroke, multiple sclerosis, hypertension, diabetes, ischemic heart disease, osteoarthritis. The active development of the ^{23}Na MRI is promoted by the growth of available magnetic fields, the expansion of hardware capabilities, and the development of pulse sequences with ultra-short echo time.

Keywords: ^{23}Na MRI *in vivo*, quadrupolar interaction, relaxation, tissue sodium concentration.

Acknowledgements

The work was carried out in the Magnetic Tomography and Spectroscopy Laboratory of the Fundamental Medicine Faculty at Lomonosov Moscow State University with equipment of the Centre for collective usage and unique complex "Biospectrotomography" supported by RFBR grant No. 17-02-00465-A.

Introduction

Sodium plays an important role in the human body. It regulates the osmotic pressure, acid-base balance and transmembrane electrochemical gradient [1]. Sodium ions are involved in cardiac activity, transmission of nerve impulses and muscle contractions. The sodium concentration (intracellular – 10–15 mM, extracellular – 140–150 mM) is very sensitive to changes in the metabolic state of tissues and disturbance of cell membrane integrity. The flow of sodium into and out of the cells can occur through various mechanisms: voltage-controlled and ligand-dependent Na^+ channels, Na^+/Ca^{2+} exchangers, Na^+/H^+ exchangers, Na^+/HCO_3^- cotransporters, $Na^+/K^+/2Cl^-$ cotransporters, Na^+/Mg^{2+} exchangers, Na^+/K^+-ATPase [2]. The regulation of Na^+/K^+-ATPase plays a key role in the etiology of some pathological processes. For example, when the demand for ATP exceeds its formation, the intake of ATP for Na^+/K^+-ATPase will not be sufficient to maintain the low intracellular sodium concentration, as a result of which its growth will be observed [2,3]. Thus the measurement of the sodium concentration is of particular interest for obtaining additional biochemical information on the functions of healthy and injured tissues and organs.

The increase in the magnetic field strength of MR scanners, as well as gain of hardware capabilities, made it possible to shorten the time of data acquisition during ^{23}Na MRI (up to ~10–30 min) and to obtain images with a resolution of several millimeters. ^{23}Na MRI is already used *in vivo* in the studies of many tissues and organs of animals and humans, such as the brain, cartilage tissue, kidneys, heart, skeletal muscles, breast and skin.

Quadrupole moment and quadrupolar interaction

The nuclei with a spin $I > ½$ have a nonspherical charge density distribution and they are characterized by an electric quadrupole moment eQ [4,5]:

$$eQ = \int \rho r^2 \left(3\cos^2\theta - 1\right) dv, \tag{1}$$

where Q is a quadrupole moment of the nucleus, ρ is a charge density of the nucleus, r is the distance from the center of the nucleus to the volume element dv, θ is the angle between r and the nucleus spin directed along the Z axis. Q is a measure of the deviation of the electric charge distribution in the nucleus from the spherical shape. If $Q > 0$, then the charge distribution is elongated along the axis of the magnetic moment, and is flattened if $Q < 0$ (Fig. 1). Table 1 gives the values of the quadrupole moments for some nuclei.

Table 1. Quadrupole moments of some nuclei [6]

Nucleus	Q, $\times 10^{-28}$ m^2 (barn)
^{2}H	2.86×10^{-3}
^{17}O	-2.558×10^{-2}
^{23}Na	0.104
^{35}Cl	-8.165×10^{-2}
^{39}K	5.85×10^{-2}
^{59}Co	0.42
^{181}Ta	3.17

Quadrupole effects are due to the interaction of the quadrupole moment of the nucleus with the gradient of the electric field (EFG) [5]. EFG characterizes the environment of the nucleus and is composed of its nearest electronic environment, as well as from charges and the location of nuclei around it. EFG is a measure of the spatial inhomogeneity of the electrostatic potential V inside the nucleus, which is created by external charges. From the mathematical point of view, the EFG is a symmetric tensor of the 2nd rank:

$$\mathbf{V} = \nabla E_{\alpha\beta} = \begin{pmatrix} V_{xx} & V_{xy} & V_{xz} \\ V_{yx} & V_{yy} & V_{yz} \\ V_{zx} & V_{zy} & V_{zz} \end{pmatrix}. \tag{2}$$

The components of the tensor **V** are second-order derivatives of the potential V with respect to the coordinates:

$$V_{\alpha\beta} \equiv \frac{\partial^2 V}{\partial x_\alpha \partial x_\beta}, \quad x_\alpha, x_\beta = x, y, z.$$

Since the tensor **V** is symmetric, it can be diagonalized:

$$\mathbf{V} = \begin{pmatrix} V_{x'x'} & 0 & 0 \\ 0 & V_{y'y'} & 0 \\ 0 & 0 & V_{z'z'} \end{pmatrix}, \quad |V_{z'z'}| \geq |V_{y'y'}| \geq |V_{x'x'}|, \quad V_{x'x'} + V_{y'y'} + V_{z'z'} = 0. \tag{3}$$

The degree of asymmetry of the electric field gradient is characterized by the asymmetry parameter η:

$$\eta = \left| \frac{V_{y'y'} - V_{x'x'}}{V_{z'z'}} \right|, \quad 0 \leq \eta \leq 1. \tag{4}$$

For convenience, we rename the dashed coordinates: x', y', $z' \rightarrow x$, y, z. Let the electric field on the nucleus have axial symmetry, i.e. the gradient of the electric field is axially symmetric:

$V_{xx} = V_{yy} \neq V_{zz} \Rightarrow \eta = 0$. Then the energy W_Q of the charge interaction with the potential V of the electric field (quadrupole energy) is determined as follows [7]:

$$W_Q = \int \rho(x,y,z)V(x,y,z)dv = \frac{eQV_{zz}}{4I(2I-1)}\left[3m^2 - I(I+1)\right], \tag{5}$$

where m is the magnetic quantum number, $m = I, I-1, \ldots, -I+1, -I$. The interaction strength is characterized by a constant of quadrupole interaction $\chi = eQV_{zz}/h$, where h is the Planck constant. The component V_{zz} is represented in the form $V_{zz} = eq$, where q is a quantity that itself has no physical meaning [8].

The distance between the quadrupole energy levels is equal to $h\nu_Q = \hbar\omega_Q$, where ν_Q (or ω_Q) is a quadrupole frequency [8]:

$$\nu_Q = \frac{3e^2qQ}{2I(2I-1)h} = \frac{3\chi}{2I(2I-1)}, \tag{6}$$

$$\omega_Q = \frac{3e^2qQ}{2I(2I-1)\hbar}. \tag{7}$$

We assume that the quadrupole interaction is small in comparison with the interaction of the nucleus with a static magnetic field. Then the energy levels are expressed as follows [7]:

$$E_m = -\gamma\hbar B_0 m + \frac{e^2qQ}{4I(2I-1)} \cdot \frac{3\cos^2\theta - 1}{2} \cdot \left(3m^2 - I(I+1)\right), \tag{8}$$

where θ is the angle between the axis of the electric field gradient (which is assumed to be axially symmetric) and the magnetic field. The first term in formula (8) is the Zeeman energy level, the second term is quadrupole one.

If the nucleus spin is 3/2, then there are 4 possible values for m: +3/2, +1/2, –1/2, –3/2. Consequently, 4 spatial orientations are possible in the presence of the magnetic field, which correspond to the 4 possible energy levels. According to the selection rule $\Delta m = \pm 1$, transitions are allowed only between neighboring levels. In the presence of electric field gradients ($q \neq 0$), the energy levels are not equidistant, since the quadrupole interaction leads to their shift [7,9] as can be seen from the Equation (8) (Fig. 2). This phenomenon is due to the different orientations of the nucleus relative to the gradient of the electric field [10]. Under the shift, the value of the central transition remains unchanged, the 3/2 → 1/2 transition decreases by $\Delta\omega$, the –1/2 → –3/2 transition increases by $\Delta\omega$. The probability of the central transition is 40%, while the probability of each satellite transition is 30% [11].

The relaxation of nuclei with spin 3/2

The quadrupole interaction affects the relaxation rates of nuclei between energy levels. The nuclear relaxation can occur only through stimulated nuclear transitions. The fluctuating field that causes these transitions can be characterized by the correlation function $C(t)$, which describes the change in the field with time. The Fourier transform $J(\omega)$ of the function $C(t)$ describes the spectral density of the time-varying field [10].

For a system of spins 3/2 with one resonance frequency ω_0, it is shown [12] that T_1 and T_2 relaxation have two components. 80% of the total T_1 relaxation is accounted for T_1':

$$\frac{1}{T_1'} = 2\left(\frac{eQ}{\hbar}\right)^2 J(2\omega_0); \tag{9}$$

20% – for T_1'':

$$\frac{1}{T_1''} = 2\left(\frac{eQ}{\hbar}\right)^2 J(\omega_0); \tag{10}$$

60% of the total T_2 relaxation is accounted for T_2':

$$\frac{1}{T_2'} = \left(\frac{eQ}{\hbar}\right)^2 [J(0) + J(\omega_0)]; \tag{11}$$

40% – for T_2'':

$$\frac{1}{T_2''} = \left(\frac{eQ}{\hbar}\right)^2 [J(\omega_0) + J(2\omega_0)]. \tag{12}$$

Field fluctuations are due to translational and rotational movements of water molecules in the first hydration shell, with rotational motions making the main contribution to relaxation [13].

The spectral density function corresponding to the rotational motion has the following form (Fig. 3) [10]:

$$J(\omega) = \frac{(eq)^2}{20} \cdot \frac{\tau_c}{\left(1 + \omega^2 {\tau_c}^2\right)}, \tag{13}$$

where τ_c – the correlation time – is the characteristic decay time of the correlation function. τ_c is an indicator of the duration of the interaction.

Taking into account expression (13), formulas (9) – (12) can be rewritten as follows:

$$\frac{1}{T_1'} = \frac{1}{10}\left(\frac{e^2 qQ}{\hbar}\right)^2 \cdot \frac{\tau_c}{1 + 4{\omega_0}^2 {\tau_c}^2} \quad (80\%) \tag{14}$$

$$\frac{1}{T_1''} = \frac{1}{10}\left(\frac{e^2 qQ}{\hbar}\right)^2 \cdot \frac{\tau_c}{1 + {\omega_0}^2 {\tau_c}^2} \quad (20\%) \tag{15}$$

$$\frac{1}{T_2'} = \frac{1}{20}\left(\frac{e^2qQ}{\hbar}\right)^2 \cdot \left(\tau_c + \frac{\tau_c}{1+\omega_0{}^2\tau_c{}^2}\right) \quad (60\%) \tag{16}$$

$$\frac{1}{T_2''} = \frac{1}{20}\left(\frac{e^2qQ}{\hbar}\right)^2 \cdot \left(\frac{\tau_c}{1+\omega_0{}^2\tau_c{}^2} + \frac{\tau_c}{1+4\omega_0{}^2\tau_c{}^2}\right) \quad (40\%) \tag{17}$$

For free ions, $\tau_c \approx 10^{-11}$ s. Taking into account that resonance frequencies ~100 MHz at high magnetic fields, we obtain $\tau_c << 1/\omega_0$ [10]. Then:

$$\frac{1}{T_1'} = \frac{1}{T_1''} = \frac{1}{T_2'} = \frac{1}{T_2''} = \frac{1}{10}\left(\frac{e^2qQ}{\hbar}\right)^2 \tau_c, \tag{18}$$

i.e. all the relaxation times are equal to each other.

The bound ions have a long τ_c: $\tau_c \geq 1/\omega_0$. This case is characterized by two different values of T_2 and two different values of T_1 [10]. Due to the small fraction of the short component T_1' (20%), T_1 relaxation is often considered to be mono-exponential in an MR experiment [14].

The spectra of nuclei with spin 3/2

In the case when a sample with a very short correlation time ($\tau_c << 1/\omega_0$, extreme narrowing regime), such as a pure aqueous solution with rapidly rotating molecules, is considered, relaxation times T_2 will be relatively long, and therefore one narrow peak will be seen in the MR spectrum (Fig. 4a) [10].

As the ions become limited in motion, the correlation time increases ($\tau_c \approx 1/\omega_0$) and, consequently, the relaxation times of the nuclei decrease, with 60% of the nuclei being more prone to this phenomenon than the remaining 40%. Thus in this case there will be a superposition of two resonances in the spectrum, with a narrow resonance peak containing 40% of energy, and a wide resonance peak containing 60% of energy (Fig. 4b) [10].

If the correlation time is very long ($\tau_c >> 1/\omega_0$), the quadrupolar interaction has a stable effect on the energy levels and the spectrum is represented by three separated resonance peaks (Fig. 4c) [10].

NMR properties of ^{23}Na nuclei

The natural abundance of the NMR active isotope ^{23}Na is 100%. The gyromagnetic ratio of the sodium nuclei γ = 11.262 MHz/T. Its Larmor frequency is ≈5% higher than the frequency of the ^{13}C nucleus and is ≈26% of the proton frequency. ^{23}Na has a spin of 3/2 and, consequently, has a nuclear quadrupole moment. The sodium NMR sensitivity is 9.2% of the proton NMR sensitivity, and the sodium concentration *in vivo* is on average ≈2000 times less than the concentration of water protons. Therefore ^{23}Na MRI has a signal-to-noise ratio (SNR) ≈(6–16)×10^3 times lower

than the ^{1}H MRI SNR. In biological tissues, the interaction of the quadrupole moment with the electric field gradients created by the electronic environment of the nucleus leads to a biexponential T_2 relaxation. The short T_2 component $T_{2,fast}$ = 0.5–5 ms gives a 60% contribution to the MR signal, the long T_2 component $T_{2,slow}$ = 15–30 ms corresponds to 40% of the signal. Table 2 shows the concentration and relaxation times of ^{23}Na nuclei in different biological tissues. To detect both components of transverse relaxation, it is necessary to use pulse sequences with an ultrashort echo time (TE<0.5 ms).

It is worth noting that there is a broad range of published sodium concentrations and relaxation times. This variability is likely caused by systematic errors in the MR experiments and by measurement techniques rather than by physiological difference in different subjects. The possible reasons for the wide spread of the values include partial volume effects [15], B_0 and B_1 fields inhomogeneities [16,17], different data acquisition and quantification schemes in ^{23}Na MR studies. In addition, T_1 and T_2 parameters increase with the static magnetic field strength B_0 in case when the spin system is outside the extreme narrowing regime [18].

Table 2. The values of the concentration and relaxation times of 23Na nuclei in biological tissues [19]

Tissue	[Na^+], mM	T_1, ms	$T_{2,fast}$, ms	$T_{2,slow}$, ms
Brain white matter	20 – 60	15 – 35	0.8 – 3	15 – 30
Brain grey matter	30 – 70	15 – 35	0.8 – 3	15 – 30
Cerebrospinal fluid	140 – 150	50 – 55	-	55 – 65
Cartilage	250 – 350	15 – 25	0.5 – 2.5	10 – 30
Blood	140 – 150	20 – 40	2 – 3	12 – 20
Muscle	15 – 30	12 – 25	1.5 – 2.5	15 – 30

Potential medical applications of ^{23}Na MRI

The excellent reviews of potential biomedical applications of ^{23}Na MRI in humans are presented in [19,20]. The authors of [21] elucidated the methodological aspects of ^{23}Na MRI. In our review, we focused on the potential medical applications of ^{23}Na MRI in humans, complementing the existing recently made reviews and also paying attention to the acquisition parameters used in ^{23}Na MR studies.

Brain

Alzheimer's disease

In [22], ^{23}Na MRI of the brain of 5 people with mild form of Alzheimer's disease (mAD) and 5 healthy volunteers (control group) was performed. The diagnosis was carried out at 3 T field using

the quadrature ^{23}Na birdcage coil for the head and the fast gradient echo (GRE) pulse sequence with parameters: field of view (FOV) = 245×245 mm^2, matrix size (MTX) = 64×64, slice thickness (ST) = 10 mm, repetition time (TR) = 9.13 ms, echo time (TE) = 2.96 ms, flip angle (FA) = 60°, 18 slices, nonselective excitation pulse of 1 ms duration, bandwidth (BW) = 130 Hz/pixel, number of scans (NS) = 210, acquisition time (TA) = 20 min. The authors note a 7.5% increase ($P<0.01$) of the signal intensity (SI) in patients with mAD (68.25%±3.4%) compared with the SI in healthy volunteers (60.75%±2.9%). The negative correlation was found between the increase in SI and the volume of the hippocampus (group with mAD: 3.22±0.50 cm^3, control group: 3.91±0.45 cm^3, r^2 = 0.5).

Huntington's disease

In [23], ^{23}Na MRI of the brain of 13 people with Huntington's disease and 13 healthy volunteers was performed. The study was carried out at 4 T field using the ^{23}Na/^{1}H transceiver RF coil and single-point ramped imaging with T_1 enhancement (SPRITE) pulse sequence [24,25] with parameters: short nonselective RF excitation pulse, TE_{eff} = 300 μs, FOV = 256×256×256 mm^3, MTX = 64×64×64, FA = 4°, TA = 36 min. People with Huntington's disease had an increase of tissue sodium concentration (TSC) in the brain both in general and in various regions of the brain. The largest increase was observed in the caudate nuclei, the key region of the brain in Huntington's disease (72±7 in the group with pathology, 52±6 in the control group, $P<0.001$). The authors point out the presence of relation between TSC enhancement and gray matter atrophy in the majority of brain regions. In the hippocampus, insula, temporal and occipital lobes, the increase in TSC is observed with no changes in the gray matter volume, from which it can be assumed that TSC can serve as an early marker of metabolic changes in brain tissue.

Multiple sclerosis

There is a good review of ^{23}Na MRI clinical studies conducted on patients with multiple sclerosis [26]. In our work, we highlight some clue works made in this field.

The paper [27] is devoted to the study of the brain of patients with multiple sclerosis of relapsing-remitting (RR MS) type by the ^{23}Na MRI method. A survey of 17 patients and 13 healthy volunteers (control group) was performed. The measurements were carried out at 3 T field using the ^{23}Na/^{1}H transceiver volume RF head coil and the 3D radial GRE pulse sequence with parameters: TR/TE = 120/0.05 ms, 1440 projections, FA = 90°, NS = 5, BW = 130 Hz/pixel, FOV = 240×240 mm^2, MTX = 60×60, spatial resolution = 4×4×4 mm^3, TA = 16 min. In the control group, TSC in the cerebellum and splenium of the corpus callosum was higher than in the periventricular regions ($P = 0.0006$ and $P = 0.0004$). In the gray matter of the brain, TSC was

higher than in the white matter (P<0.0001). T_1-weighted ^{1}H MRI was performed for patients after the injection of Gd-contrast. The affected areas with a diameter greater than 5 mm were considered. Based on the T_1-weighted MR images obtained, the lesion sites were divided into contrast-enhanced and non-enhanced, the latter including T_1-iso- and hypo-intensive foci. TSC was assessed in 4 contrast-enhanced, 25 iso-intensive and 67 hypo-intensive lesions. The TSC level in the hypo-intensive zones did not statistically differ from TSC in contrast-enhanced zones, but was higher compared with TSC in iso-intensive zones (P<0.0001) and regions of normal white matter (P<0.0001). TSC in iso-intensive foci was higher than in frontal (P = 0.009) and periventricular normal white matter (P = 0.007), but lower than in normal gray matter (P<0.0001). Since TSC is the weighted average of extra- and intracellular sodium in the tissue of interest, the increase in TSC in patients with multiple sclerosis may reflect both extracellular expansion due to vasogenic edema, cell death or demyelination, and an increase in intracellular sodium concentration due to overexpression of sodium channels or hypercellularity.

The purpose of work [28] was to quantify brain sodium accumulations and characterize the spatial location of sodium abnormalities at different stages of RR MS using ^{23}Na MRI. The subjects of study were 3 groups: 14 patients with early stage of RR MS, 12 patients with advanced stage of RR MS, and 15 healthy controls. MR studies were performed at 3 T field. ^{23}Na MRI was carried out using ^{23}Na/^{1}H volume head coil and density-adapted 3D radial projection reconstruction (DA 3D RPR) [29] pulse sequence with parameters: TR/TE = 120/0.2 ms, 17000 projections, 369 samples per projection, radial fraction *p* of 0.2 not sampled with density adaption, readout time per spoke = 20 ms, FA = 87°, spatial resolution = 3.6×3.6×3.6 mm^3, TA = 34 min. ^{1}H MRI was used to obtain reference anatomical images. TSC values in white matter (WM) T_2 lesions were higher for early RR MS (median = 55.9 mM, range = 46.9–69.2 mM, P = 0.007) and advanced RR MS (median = 59.7 mM, range = 50.2–65.7 mM, P<0.0001) compared with values from WM of controls (median = 48.8 mM, range = 40.3–55.6 mM). In normal-appearing (NA) WM, TSC values were higher in patients with advanced RR MS (median = 54.4 mM, range = 48.6–58.8 mM) than in controls (median = 48.8 mM, range = 40.3–55.6 mM, P=0.007). In gray matter (GM), TSC values were higher in patients with advanced RR MS (median = 61.1 mM, range = 54.8–64.1 mM) relative to TSC in patients with early RR MS (median = 56.2 mM, range = 51.2–62.4 mM, P = 0.044) and in controls (median = 53.5 mM, range = 44.7–61.8 mM, P = 0.004). Statistical mapping analysis performed by the authors showed confined TSC increase inside the brainstem, cerebellum and temporal poles in early RR MS and widespread TSC increase that affected the entire brain in advanced RR MS. Patients' disability was correlated with TSC increase inside motor networks. The authors supposed that the detected abnormal sodium accumulation in WM lesions may be caused by either the extracellular or intracellular sodium

content increase or both of them. The former, if present, can be related to edema or loss of tissue. The intracellular sodium increase may be explained by demyelination or gliosis processes. The diffuse sodium accumulation confirmed by the increased levels of TSC in NAWM and GM at the advanced stage of RR MS may reflect the progressive axonal injury. The authors hypothesized that the highly connected brain regions, such as brainstem, cerebellum and temporal poles, suffered from energy failure induced by an imbalance between energy supply and energy demand. The abnormal sodium accumulation in all brain regions at the advanced stage of RR MS may be related to the progression of diffuse inflammation outside the macroscopic WM lesions.

In [30], the authors concentrated on the problem of separation of two compartments, intra- and extracellular sodium, in the structures of the brain of patients with RR MS. The group of patients consisted of 19 people, the control group consisted of 17 people without diseases. The studies were carried out at 3 and 7 T fields to obtain ^{1}H and ^{23}Na MR images, respectively. ^{23}Na MRI was performed using the ^{23}Na/^{1}H transceiver RF head coil and two pulse schemes – single-quantum (SQ) and triple-quantum filtering (TQF) [31–44]. To collect data in the case of SQ ^{23}Na MRI, the 3D GRE pulse sequence [45] was used with parameters: TR/TE = 150/6.8 ms, FA = 90°, FOV = 240×240 mm^2, MTX = 48×48, voxel size = 5×5×5 mm^3. The TQF scheme was implemented by applying the modified 3D GRE pulse sequence with a 12-step phase cycle and parameters: TR/TE = 150/6.8 ms, FA = 90°, FOV = 240×240×240 mm^3, MTX = 30×30×24, voxel size = 8×8×10 mm^3, τ_1 = 6.8 ms, τ_2 = 150 ms, NS = 2. Quantitative analysis performed by the authors showed the increase in TSC and ISC (intracellular sodium concentration) and the decrease in ISVF (intracellular sodium volume fraction) in the brain gray and white matter of patients. The correlation was established between the volume of lesions on T_2-weighted ^{1}H images and TSC in the corticospinal tract, the right anterior cingulate gyrus and the right precentral gyrus (r = 0.47–0.71), and also with ISVF in the right postcentral gyrus (r = –0.59). The volume of lesions on T_1-weighted ^{1}H images correlated with TSC in the corticospinal tract, right precentral gyrus, right anterior cingulate gyrus and thalamus (r = 0.50–0.63), as well as with ISVF in the corticospinal tract (r = –0.55) and anterior cingulate gyrus (r = –0.70). The authors argue that the decrease in ISVF reflects an increase in extracellular volume that is associated with cell death and tissue atrophy, whereas the increase in ISC reflects a disruption of cellular metabolism associated with dysfunction of mitochondria and ion channels.

Stroke

In [46], the authors conducted a multimodal study of the brain *in vivo* in 9 patients with ischemic stroke 4–32 hours after the symptoms onset. The results of ^{23}Na MRI, ^{1}H perfusion-weighted (PW) and diffusion-weighted (DW) MRI were compared. ^{1}H PW and DW MRI were performed on a

1.5T scanner, ^{23}Na MRI was performed at 4.7 T field. ^{23}Na MR images were obtained using the ^{23}Na birdcage RF coil and the projection acquisition in the steady-state for sodium imaging (Na-PASS) [47] pulse sequence with parameters: TR/TE = 25/0.6 ms, FA = 55°, voxel size = 2.4×2.4×4.8 mm^3, TA = 10 min. The qualitative analysis carried out by the authors showed the increase in the ^{23}Na MR SI in zones with limited diffusion, whereas no changes in the ^{23}Na SI were observed in the penumbra region. The quantitative analysis revealed no statistically significant differences between the ^{23}Na SI in the penumbra and the homologous contralateral region at different times after the stroke onset. Conversely, the ^{23}Na SI in the lesion focus identified on the DW images increased with the passage of time after stroke, what in combination with a decrease of the water apparent diffusion coefficient (ADC) was believed to reflect ATPase dysfunction or cell integrity disorder. The absence of changes in the sodium content in the penumbra, according to the authors, speaks about the preservation of ion homeostasis in this region and it is consistent with the invariability of ADC.

The aim of work [48] was to evaluate the changes in TSC and T_2^* time of ^{23}Na nuclei in the brain of 4 mice after thromboembolic stroke. The study was conducted at 9.4 T field using ^{23}Na surface RF coil. The data was collected using the 3D chemical shift imaging (CSI) pulse sequence with parameters: TR = 25, 60 ms, MTX = 47×47×37, 39×39×33, FOV = 19.2×19.2×38.4 mm^3, spatial resolution = 0.6×0.6×1.2 mm^3, TA = 14 (for one mouse), 65 min (for other 3 mice). The ^{23}Na SI in the infarction zones was 160–250% higher than in the contralateral areas of the brain. The T_2^* times of ^{23}Na nuclei in the lesions were 5–72% higher than in the contralateral intact tissues.

Brain tumors

In [49], the study of 20 patients with a malignant brain tumor and 9 healthy volunteers was conducted. 17 patients suffered from astrocytoma, 3 patients – from oligodendroglioma. ^{23}Na and ^{1}H MRI were performed at 1.5 T field. Excitation of ^{23}Na nuclei and reception of the RF signal was carried out with use of the 16-element ^{23}Na birdcage RF coil. To acquire data, the authors used the 3D twisted projection imaging (TPI) pulse sequence [16,50,51] with parameters: 90° pulse of 0.4 ms duration, TR/TE = 120/0.37 ms, 1240 projections, NS = 6, TA ≈15 min, FOV = 22×22×22 cm^3, MTX = 64×64×64, voxel size = 0.34×0.34×0.34 mm^3. Measurements of T_1 time in the brain of a healthy volunteer gave the following results: 11.2±0.4 ms for gray matter (GM), 16.9±0.3 ms for white matter (WM), 20±2 ms for cerebrospinal fluid (CSF), 26±5 ms for vitreous body. TSC in tumors was comparable with TSC in the vitreous body, 1.6 times higher than in GM ($P<0.001$), 1.4 times higher than in WM ($P<0.001$), 1.4 times higher than in contralateral tissue ($P<0.002$), and 25% lower than in CSF ($P<0.001$). According to the authors opinion, the growth

of TSC in malignant tumors reflects both changes in the volume of extracellular space, and in the intracellular sodium concentration $[Na^+]_{in}$. In the presence of malignant neoplasm, the activity of Na^+/K^+-ATPase was decreased and the kinetics of Na^+/H^+ exchangers was violated, what led to an increase of $[Na^+]_{in}$. Neovascularization of the tumor and expansion of its interstitial space lead to an increase in the volume of extracellular fluid and they are associated with the tumor ability to proliferate.

In [52], the effectiveness of the ^{23}Na MRI method consisted in the simultaneous application of two data collection schemes, SQ and TQF – SISTINA, is shown. For the study, 3 patients with a brain tumor and 6 healthy volunteers were selected. To carry out ^{23}Na MR measurements, a protocol was compiled with parameters: FOV = 320×240×220 mm^3, MTX = 32×24×22, TR = 100 ms, τ = 6000 μs, δ = 40 μs, TE = 0.26, 7.0, 16.2, 25.4, 34.6, 43.8 ms, BW = 13.44 kHz, 13500 projections, 120 Hz/pixel, NS = 36, RF pulse duration = 500 μs, TA = 24 min. ^{23}Na MRI was performed at 4 T field using ^{23}Na/^{1}H birdcage RF coil. The authors also used PET with O-(2-[^{18}F]fluoroethyl)-L-tyrosine aminoacid as a tracer, and standard ^{1}H MRI (3 T) for comparison with ^{23}Na MR images. SQ images showed an increase in SI in tumors, while TQF images showed a decrease in SI. The latter indicates that Na^+ ions in the lesions are more mobile than in intact tissue. The ^{23}Na MRI results were consistent with the contrast changes in ^{1}H MR images. PET images showed high uptake of aminoacids in the tumor and presented sharp edges.

The authors of [53] aimed at monitoring the response to chemotherapy of mouse xenograft tumors propagated from human prostate cancer cell lines. ^{23}Na MRI was performed at 4.23 T using small quadrature birdcage coil and inversion-recovery (IR) pulse sequence with parameters: TR/TE = 100/5.6 ms, FOV = 40 mm, ST = 2.5 mm, inversion time (TI) = 25 ms, FA = 90°, MTX = 64×64×8. The inversion pulse suppresses signal from sodium with long T_1 relaxation times, weighting the image toward intracellular sodium nuclei. Comparing the weighted ^{23}Na MR images before and after 24 h after administration of antineoplastics, the authors measured a 36±4% ($P<0.001$, n=16) increase in SI. This increase was explained by the increase of intracellular sodium concentration. The authors also found the inverse correlation between tumor proliferation reduction after drug administration and ^{23}Na MR image response on a tumor-to-tumor basis ($P<0.02$, n=10).

The objective of work [54] was to investigate the relaxation-weighted ^{23}Na MR signal (^{23}NaR) of brain lesions and the potential of a combined use of ^{23}Na spin-density weighted (^{23}NaT) and ^{23}NaR imaging for tumor characterization. 7 healthy subjects and 16 patients suffering from singular supratentorial brain tumors (14 WHO grade I–IV and 2 metastases) were examined. ^{23}Na MR images were acquired at 7 T field using ^{23}Na/^{1}H quadrature birdcage coil. All ^{23}Na MRI sequences used were based on the DA 3D RPR pulse sequence. Here we indicate some methods

used in [54] with the corresponding acquisition parameters. ^{23}NaT MR images with 2.5×2.5×2.5 mm^3 spatial resolution were obtained using the following parameters: TR/TE = 25/0.5 ms, FA = 55°, readout time (T_{RO}) = 20 ms, TA = 13 min 20 s. To further differentiate the ^{23}NaT signal, two ^{23}NaR methods were applied. The 1st method used an IR preparation pulse to exploit T_1-differences of Na^+, the parameters were: TR = 185 ms, TI = 41 ms, TE = 0.6–0.8 ms, spatial resolution = 5.5×5.5×5.5 mm^3, T_{RO} = 10 ms, TA = 10 min. The 2nd method was based on ^{23}Na multiecho sequences to exploit differences in T_2^* relaxation times, the parameters of fast sequence were: 2 echoes, TR/TE_A/TE_B = 30/0.6/13 ms, FA = 68°, spatial resolution = 5×5×5 mm^3, T_{RO} = 10 ms, TA = 2.5 min. ^{23}NaT MRI showed increased signal intensities in 15 of 16 brain tumors before therapy. ^{23}NaR MRI allowed further differentiation of the detected lesions: all glioblastomas demonstrated higher ^{23}NaR signal intensities relative to WHO grade I–III tumors. Moreover, unlike the ^{23}NaT, the ^{23}NaR signal correlated with the MIB-1 proliferation rate of tumor cells.

The aim of work [55] was to evaluate the ability of ^{23}Na MRI in differentiation of brain tumors. 34 patients with glioma WHO grades I–IV were examined. ^{23}Na MRI was carried out at 7 T field using ^{23}Na/^{1}H quadrature birdcage coil with an inner coil diameter of 26 cm. To obtain ^{23}Na MR images, two methods based on DA 3D RPR scheme were applied: spin-density weighted (^{23}NaT) and relaxation-weighted (^{23}NaR). The acquisition parameters of ^{23}NaT approach were: TR/TE = 160/0.35 ms, T_{RO} = 10 ms, spatial resolution = 3.0×3.0×3.0 mm^3, TA ≈ 10 min. ^{23}NaR approach was realized with IR pulse sequence with parameters: TR/TE = 185/0.75 ms, TI = 41 ms, T_{RO} = 185 ms, spatial resolution = 4.4×4.4×4.4 mm^3, TA ≈ 10 min. The authors demonstrated that the ^{23}NaR/^{23}NaT ratio of a treatment-naïve brain tumor is a significant predictor of isocitratedehydrogenase (IDH) mutation status ($P<0.001$) and progression-free survival ($P<0.003$). Furthermore, ^{23}Na MRI allows to classify tumors noninvasively. ^{23}NaR/^{23}NaT quantity of contrast-enhancing tumor portions promotes differentiation among most glioma types ($P<0.001$).

In [56], the combined use of two diagnostic modalities was presented. Two patients suffered from glioblastoma multiforme (GBM) underwent dynamic [^{18}F]fluorothymidine (F-18 FLT) PET and 3T ^{23}Na MRI scans at baseline (before therapy), at an early time point after beginning therapy (ETA – early therapy assessment) and at a late follow-up time point after therapy (LTA – late therapy assessment). ^{23}Na MRI was performed with ^{23}Na/^{1}H dual-quadrature four-port birdcage RF coil and TPI pulse sequence, each ^{23}Na image (Fig. 5) was acquired in 10 min. In patient 1, the average tumor sodium concentration was 74 mM at ETA time point and 96 mM at LTA time point, and the F-18 FLT tracer distribution volume (V_d) was 0.80 and 0.99 at ETA and LTA time points, respectively. In patient 2, the average tumor sodium concentration was 58 mM, 59 mM and 57 mM, and V_d was 0.63, 0.74 and 0.65 at baseline, ETA and LTA time points, respectively. The

uptake of the PET tracer F-18 FLT is expected to correlate with cellular proliferative activity [56]. ^{23}Na MRI has a great potential for the study of brain neoplasms because the cell membrane depolarization that precedes the large degree of cell division in the neoplastic tissue leads to an increase in the intracellular sodium concentration and a concomitant rise in the total TSC [56]. The authors showed that while both modalities independently revealed voxel-wise changes in tissue status in course of time, which may be related to therapy, ^{23}Na MRI and F-18 FLT PET may provide complementary information regarding tumor progression and response.

The comparison study using ^{23}Na MRI and ^{35}Cl MRI of brain tumors was performed by the authors of [57]. ^{23}Na and ^{35}Cl nuclei are similar in sense of their quadrupolar nature (I = 3/2). Cl^- is the important ion involved in many physiological processes, such as the inhibition of muscular and neuronal cells. It also takes part in cell volume regulation and cell migration in cancer. 7T ^{23}Na MRI and ^{35}Cl MRI were conducted for one patient with GBM. The ^{23}Na/^{1}H and ^{35}Cl/^{1}H quadrature birdcage coils were used. ^{23}Na and ^{35}Cl MR images were acquired using DA 3D RPR technique with isotropic spatial resolution. Within the affected tissue, concentration-weighted ^{23}Na and ^{35}Cl MRI revealed increased signal intensities. However ^{23}Na IR MRI and ^{35}Cl IR MRI showed different SI behavior: ^{23}Na IR SI decreased in the affected brain region, and ^{35}Cl IR SI was ≈2 times higher than in normal brain tissue.

Breast

The possibility of using ^{23}Na MRI in breast cancer was shown in [58]. 19 women with a malignant breast tumor and 3 women with a benign tumor were examined. ^{23}Na MRI was performed at 1.5 T field using the solenoidal ^{23}Na RF coil placed inside the ^{1}H RF phase array coil and the TPI pulse sequence with parameters: adiabatic excitation pulse, FA = 90°, TR/TE = 100/0.4 ms, NS = 6, number of projections = 1240, TA = 12:24 min, isotropic spatial resolution = 6 mm (voxel volume = 0.22 ml). Mean TSC in malignant tumors was greater (53±16 mM) than TSC in benign tumors (26±5 mM) ($P<0.0004$). TSC in undamaged glandular tissue was approximately equal to TSC in benign tumors and equals 34±13 mM.

The results of ^{23}Na MRI of a mammary gland in a healthy woman are presented in [59]. The measurements were carried out at 3 T field. To determine the TSC, the authors used the ^{23}Na volume birdcage RF resonator and the ^{23}Na receiver surface RF coil. ^{23}Na MR images were obtained using the DA 3D RPR pulse sequence with parameters: TR/TE = 150/0.5 ms, FA = 60°, TA = 45 min. TSC in the breast tissue was 55±13 mM. Comparing this result with the TSC value obtained in [58], one can see a significant difference in the concentrations obtained. This indicates the need for further research to develop a more accurate method for determining TSC in breast tissue, what will allow the differentiation between damaged and healthy tissue.

Lungs

In [60], multimodal diagnosis of lung cancer in humans using ^{23}Na MRI, ^{1}H MRI, CT and [^{18}F]fluorodeoxyglucose (F-18 FDG) PET-CT was performed. MR studies were performed at 3 T field using the two-resonant ^{23}Na/^{1}H RF coil and the DA 3D RPR pulse sequence. ^{23}Na MRI of a 62-year-old man with an adenocarcinoma of the left upper lobe (Fig. 6), performed 1 day after the fourth cycle of Carboplatin, Gemcitabin and Cetuximab therapy, showed a low intensity of the ^{23}Na signal in the infero-lateral margin of the tumor (0.4×10^3), i.e. low viability of this part of the tumor, whereas a high SI (12.0×10^3) was recorded in the viable part of the tumor. These results were consistent with the results of F-18 FDG PET-CT (Maximum standardized uptake value (SUV_{max}) = 43 in the viable tumor margin). In addition, the central tumor showed high ^{23}Na SI due to extensive central necrosis that was confirmed by F-18 FDG PET-CT and also by homogeneous hypodensity on the CT image with contrast enhancement. ^{23}Na MRI of a 50-year-old woman with an adenocarcinoma of the right upper lobe, conducted before and 1 day after initiation of combination therapy, revealed a heterogeneous SI of the tumor suggesting heterogeneous viability of the tumor. Between the two exams the ^{23}Na SI of the tumor and the ratio of SI between the tumor and the cerebrospinal fluid (CSF) slightly increased indicating early treatment effects within the tumor. ^{23}Na MRI of lungs in conjunction with ^{1}H MRI provides functional information on the viability of the tumor before, during and after therapy. Early detection of ineffectiveness of therapy by ^{23}Na MRI will allow to correct the treatment strategy. Based on the correlation with ^{1}H MRI, CT and F-18 FDG PET-CT, the authors demonstrated the possibility of differentiation between viable tumor tissue and necrosis by the ^{23}Na MRI method. Detection of tumor heterogeneity and identification of biologically active tumor regions plays an important clinical role in the planning of intensity-modulated radiotherapy. The authors also showed that ^{23}Na MRI can visualize very early functional changes of the tumor, induced by therapy.

Heart

In [61], TSC was determined in the heart of 20 patients with non-acute myocardial infarction. The investigations were carried out at 1.5 T field using the square ^{23}Na surface RF coil and the 3D TPI pulse sequence with parameters: TR = 100, 85 ms, TE = 0.4 ms, 1240 projections, isotropic spatial resolution = 6 mm, voxel volume = 0.2 ml, TA = 12–20 min. The mean TSC in the myocardial infarction zone (59±10 μmol/g wet weight) was 30% higher than in the intact regions (left ventricle, 45±5 μmol/g wet weight, $P<0.001$). The growth of TSC did not correlate with the time interval after the infarct, functional and morphological parameters of the heart.

In [62], ^{23}Na MRI of the heart of 3 healthy volunteers was performed. The study was conducted at 7 T field using the array of ^{23}Na/^{1}H RF coils. For the construction of ^{23}Na MR images, two

protocols were used. Short-axis projections and four-chambered cardiac views were obtained using the 3D FLASH method with parameters: TR/TE = 28/1.91 ms, MTX = 64×48, voxel size = 5×5×15 mm^3, NS = 35, BW = 120 Hz/pixel, FA = 28°, TA ≈ 6 minutes. The whole heart coverage ^{23}Na data sets were collected using the DA 3D RPR pulse sequence with parameters: TR/TE = 11/0.4 ms, T_{RO} = 7.1 ms, FA = 36°, 104 projections, NS = 10, voxel size = 6×6×6 mm^3, TA ≈ 18 min. ^1H MRI was performed using the 2D cine-FLASH method. To synchronize the collection of ^{23}Na and ^1H data with the cardiac cycle, an acoustic gating device was used. The results of the application of the 1st protocol were: SNR = 15±4 in the blood pool, SNR = 10±3 in the myocardium. The 2nd protocol gave the following SNR values: 38±4 in the blood pool, 25±4 in the myocardium. The authors note that ^{23}Na MRI in the field of 7 T can be used in the assessment of sodium homeostasis and myocardial viability, in the study of cardiac channelopathies, as well as hypertrophic cardiomyopathy.

Abdomen

Kidneys

An excellent review about ^{23}Na MRI of kidney is presented in [63]. Here we emphasize several works.

In [64], mapping of sodium distribution in the human kidney and a quantitative assessment of the corticomedullary gradient of sodium ions were carried out. The objects of the study were 6 volunteers. ^{23}Na MR images were obtained at 3 T field using the quadrature surface ^{23}Na RF coil. The data was collected using the 3D GRE pulse sequence with the following parameters: FOV = 38×38×24 cm^3, MTX = 128×128×16, TR/TE = 30/1.8 ms, NS = 24, TA = 25 min, t_{RF} = 300 μs (nonselective pulse), spatial resolution = 0.3×0.3×1.5 cm^3. There was a linear increase of SNR in the direction from the cortical layer of the kidney to the medullary substance with the average slope of 1.6±0.2 (relative units / mm), after what a decrease of SNR toward the renal pelvis was noted. The 12-hour water deprivation led to an increase in the corticomedullary gradient by 25% ($P<0.05$).

The authors of [65] performed 7T ^{23}Na MRI of the kidneys of 8 healthy volunteers. The corticomedullary sodium gradient and transverse relaxation times (T_2^*) were measured. For transmission and reception of the RF signal, the 6-channel array of coils tuned only to the ^{23}Na frequency was used. ^{23}Na MR images were obtained using the 3D gradient echo with variable TE (vTE-GRE) pulse sequence with parameters: spatial resolution = 4×4×5 mm^3, FOV = 256×256 mm^2, MTX = 64×64, number of slices = 24, TE = 4.19 ms, average TR = 49 ms, BW = 30 Hz/pixel, average NS = 34, mean TA ≈ 42 min. To build T_2^* maps, the multi-echo 3D vTE-GRE sequence with 10 different TE values (from 2.64 to 60.42 ms) was applied. The average SNR (in arb. units

/ mm) grew along the gradient from the cortical layer of the kidneys (32.2±5.6) to the medullary substance (85.7±16.0). The mean T_2^* were different ($P<0.001$) for the cortical layer (17.9±0.8 ms) and the medullary substance (20.6±1.0 ms).

In [66], a corticomedullary sodium gradient was determined in 4 patients with central diabetes insipidus (CDI) before and after taking 20 μg of desmopressin (DDAVP). The study was conducted at 3 T field using the 8-channel ^{23}Na RF heart coil with 320×320 mm^2 coverage and the DA 3D RPR pulse sequence with parameters: TR/TE = 120/0.55 ms, 8000 projections, spatial resolution=5.0×5.0×5.0 mm^3. The mean concentration [^{23}Na] increased along the corticomedullary gradient from the cortical layer of the kidney (38.0±6.3 mM before DDAVP, 30.7±3.5 mM after) to the medullary substance (71.6±14.8 mM before DDAVP, 59.7±10.8 mM after). The decrease of [^{23}Na] on the average for the group of patients after the DDAVP administration was 17.1±1.1%. Before the DDAVP administration, the urine concentration mechanism seeks to compensate for the loss of diluted urine. The DDAVP administration increases the reabsorption of water and sodium in the collecting ducts of the kidneys, eliminating the need for the compensatory mechanism and possibly reducing renal [^{23}Na] along the corticomedullary gradient. ^{23}Na MRI can detect this change (Fig. 7), show desmopressin-controlled water reabsorption in collecting ducts and dilution of intracellular sodium.

The goal of [67] was to determine the effect of renal denervation on TSC in the kidney. The subjects of the study were 2 patients with drug-resistant hypertension. ^{23}Na MRI and ^{1}H DW MRI were performed 1 day before denervation and 1, 30 and 90 days after. ^{23}Na MR images were obtained at 3 T field using the array of ^{23}Na/^{1}H RF transceiver coils and the 3D DA RPR pulse sequence. There were no statistically significant changes in the values of ADC in the kidneys and corticomedullary ^{23}Na gradient after denervation. The authors conclude that TSC can't be selected as a reliable marker of the effectiveness of therapy. However, it is necessary to take into account the small sample in this study.

Prostate

In [68], the TSC and ADC values in the prostate gland in 8 healthy volunteers were determined. The study was carried out at 3 T field using the ^{23}Na RF transceiver heart coil with 320×320 mm^2 coverage and the DA 3D RPR pulse sequence with parameters: TR/TE = 120/0.55 ms, FA = 85°, 8000 projections, TA = 16 min, spatial resolution = 5.0×5.0×5.0 mm^3. The mean TSC in the central part of the prostate gland was 55±15 mM, while in the peripheral part – 69±16 mM. The correlation was found between the TSC and ADC parameters (r = 0.87).

The result of the study [69] was the measurement of TSC in the prostate gland of 3 patients with prostate cancer diagnosed by biopsy. ^{23}Na MRI was performed at 3 T field using the volume

quadrature transmitter RF birdcage resonator and the endorectal linear surface RF receiver coil. To obtain ^{23}Na MR images, the 3D fast GRE pulse sequence was applied with parameters: TR/TE=80/1.77 ms, rectangular excitation pulse, FOV = 14×14 cm^2, FA = 85°, ST = 6 mm, number of slices = 18, NS = 6, TA = 4 min 37 s. The mean TSC in the central part of the prostate gland was 60.2±5.7 mM, and in the peripheral part – 70.5±9.0 mM. Comparing these values with the results of [68], we can see that they coincide within the error. Therefore, the differentiation between healthy and damaged prostate tissue requires further study.

Uterus

In [70], ^{23}Na MRI and ^{1}H DW MRI were performed to monitor the treatment of uterine leiomyoma by the MRg-HIFUS method in 8 patients. Diagnostics was carried out at 1.5 T field using the ^{23}Na transceiver surface RF coil with 25×25 cm^2 coverage. ^{23}Na MRI was carried out using the 2D projection imaging pulse sequence. Parameters of the sequence: TR/TE = 100/0.2 ms, adiabatic excitation pulses of 400 μs duration, isotropic spatial resolution = 6 mm (voxel volume = 0.2 ml), FOV isotropic = 22 cm, MTX = 128×128, number of slices = 64, ST = 3.4 mm. TSC and ADC were defined. TSC in healthy tissue of myometrium was equal to 35.8±2.1 mM, in untreated leiomyomata – 28±5 mM. After treatment, TSC increased: 41.6±7.6 mM ($P<0.05$). ADC after treatment of leiomyoma was (1.30±0.38)×10^{-3} mm^2/s, what was less ($P<0.05$) compared with ADC in untreated leiomyoma (1.75±0.36)×10^{-3} mm^2/s and in healthy tissue myometrium (2.2±0.3)×10^{-3} mm^2/s.

Skeletal muscles

Diabetes

In [71], the state of the muscles of 4 patients with diabetes and 7 healthy volunteers before and after physical exertion on the muscle was assessed. ^{23}Na MRI was performed at 7 T field using the quadrature ^{23}Na RF knee coil. ^{23}Na MR images were obtained using the 3D radial GE pulse sequence with parameters: TR/TE = 80/0.16 ms, BW = 130 Hz/pixel, NS = 10, 512 projections, spatial resolution = 4×4×4 mm^3, TA ≈ 7 min. In the group of healthy volunteers (HV) and the group of patients (PAT), the ^{23}Na SI was increased in soleus (8±4%, $P = 0.028$ for HV; 10±6%, $P = 0.034$ for PAT) and gastrocnemius (13±8%, $P = 0.028$ for HV; 11±4%, $P = 0.009$ for PAT) muscles immediately after physical exertion compared with resting parameters. In the tibial muscle taken as a control, no statistically significant changes were detected (0.5±5%, $P = 0.92$ for HV; –3.6 ± 4%, $P = 0.066$ for PAT). 35 minutes after physical exertion, the ^{23}Na SI in the soleus and gastrocnemius muscles decreased to the initial level. The level of the ^{23}Na signal in the tibial muscle remained the same (–2.4 ± 5%, $P = 0.46$ for HV; –7 ± 5%, $P = 0.066$ for PAT). According

to the authors' opinion, the increase of ^{23}Na SI in soleus and gastrocnemius muscles can be caused by an increase of the total sodium content in the muscles or by changes of the T_2 time values of ^{23}Na nuclei. The authors believe that the absence of statistically significant changes in the tibial muscle may be due to the activation of physiological mechanisms of maintaining the sodium homeostasis after exercise. In addition, the recovery of the ^{23}Na signal after the load to the initial level in the PAT group was slower than in the HV group, what may be associated with a decrease of Na^+-K^+-pump activity and with a change of the tissue microvascular network in diabetic patients.

Hypertension

In [72], the study of 57 people with hypertensive disease and 56 healthy volunteers (control group) was conducted. ^{23}Na MRI was performed at 3 T field using the ^{23}Na transceiver birdcage RF knee coil. ^{23}Na MR images were obtained for the muscles and skin in the calf region using the 2D FLASH pulse sequence with parameters: TR/TE = 100/2.07 ms, FA = 90°, NS = 128, spatial resolution = 3×3×30 mm^3, TA = 13.7 min. ^{1}H MRI was performed to determine the tissue water content. The authors note an increase of the Na^+ content in the muscle tissue in men with age, whereas in women the Na^+ concentration in muscles did not change with age. There was no increase of water content in muscle tissue in men with age, despite the significant accumulation of Na^+, what indicates an increase of the anhydrous sodium concentration. In men with resistant hypertension, there was an increase of the Na^+ concentration in the muscle tissue compared with the control group. Furthermore, patients treated with spironolactone showed a decrease in muscle Na^+ concentration and a trend towards lowering blood pressure.

Muscular channelopathies

In [73], ^{23}Na MRI of the calf muscles in 6 patients with hypokalemic periodic paralysis (hypoPP), 5 patients with congenital paraomyotonia (CP) and 5 healthy volunteers was performed. ^{23}Na MR images were obtained at 3 T field using the ^{23}Na/^{1}H birdcage RF coil. Data were collected by 3 methods based on the DA 3D RPR pulse sequence. The following parameters were used for the T_1-weighted ^{23}Na MRI (^{23}Na-T_1): TR/TE = 6/0.25 ms, FA = 40°, voxel size = 5×5×5 mm^3, 14000 projections, NS = 4, TA = 5 min 36 s. To suppress the signal from free Na^+ ions, the ^{23}Na-IR MRI method was used with parameters: TR/TE/TI = 124/0.3/34 ms, voxel size = 6×6×6 mm^3, 5000 projections, TA = 10 min 20 s. The relaxation weighting was minimized by applying a short TE (0.2 ms) and a long TR (100 ms) for local TSC measurement. In this case (^{23}Na-TSC MRI), the following parameters were used: FA = 90°, 5000 projections, voxel size = 5×5×5 mm^3, TA = 8 min 20 s. TSC at rest was 24±2 mM in healthy volunteers, 27±3 mM in patients with CP and

33±5 mM in patients with hypoPP. The authors note an increase in the ^{23}Na-IR SI, a decrease in muscle strength, a trend towards the increase of the ^{23}Na-T_1 (P = 0.07) and ^{23}Na-TSC (P = 0.07) signal intensities after cooling and exercise in patients with CP, whilst statistically significant changes in the signals obtained with ^{1}H-T_2-STIR MRI weren't revealed. In the groups of patients with hypoPP and healthy volunteers, no changes were observed in ^{23}Na-T_1 and ^{23}Na-TSC signals after cooling and loading, while the growth of ^{23}Na-IR signal (more than 15%) and severe muscle edema was detected in 2 patients with hypoPP.

The work [74] is devoted to the study of hyperkalemic periodic paralysis (hyperPP) in terms of processes involving Na^+ ions. The sample consisted of 12 patients and 12 healthy volunteers, with 6 patients having permanent muscle weakness, and 6 others with episodic weakness. ^{23}Na MRI was performed at 3 T field using the ^{23}Na/^{1}H birdcage RF coil. The ^{23}Na protocol included 3 methods: ^{23}Na-TSC, ^{23}Na-T_1 and ^{23}Na-IR MRI. The parameters for each method were chosen to be the same as in [73]. At rest, the ^{23}Na-IR signal from the calf muscles was higher in patients with constant muscle weakness (0.83±0.04) than in patients with episodic weakness (0.67±0.05, P=0.002) and healthy volunteers (0.50±0.06, P<0.005). After cooling and physical exertion, there was a ^{23}Na-IR signal increase both in patients with constant weakness (from 0.83±0.04 to 0.93±0.08, P<0.005) and in patients with episodic weakness (0.68 ± 0.06 to 0.77 ± 0.06, P <0.05). In the group of healthy volunteers, ^{23}Na-IR signal did not change, muscle weakness did not arise. The ^{23}Na-T_1 signal in patients with constant weakness before and after cooling and loading was 0.89±0.07 and 0.87±0.04, respectively (P>0.99), in patients with episodic weakness – 0.72±0.10 and 0.76±0.11 (P<0.05). In the group of healthy volunteers, ^{23}Na-T_1 signal (0.55 ± 0.07 before and after cooling and load) was less than in patients (P<0.005). TSC in patients with constant weakness (40.7±3.9 μmol/g) was higher than in patients with episodic weakness (31.3±4.9 μmol/g, P=0.004) and healthy volunteers (24.3±3.4 μmol/g, P<0.005). The effectiveness of therapy was monitored for 4 patients. Acetazolamide was used for the treatment. The authors note a decrease of muscle swelling during treatment and an increase of muscle strength. Moreover, the ^{23}Na-IR MRI method showed a decrease in SI: 0.85±0.04 before therapy, 0.64±0.11 after therapy.

The objective of the study [75] was to determine whether altered Na^+ and Cl^- homeostasis inherent in the diseases such as hypoPP and Andersen-Tawil syndrome (ATS) can be visualized by means of 7T ^{23}Na and ^{35}Cl MRI. 13 patients with hypoPP were divided in 2 groups: 5 patients with the severe phenotype Cav1.1-R1239H mutation, and 8 patients with the mild phenotype Cav1.1-R528H mutation. 3 patients suffered from ATS. Control group consisted of 16 healthy volunteers. ^{23}Na and ^{35}Cl MR images of soleus muscle were obtained using ^{23}Na/^{35}Cl birdcage coil and DA 3D RPR pulse sequence. The acquisition parameters for ^{23}Na MRI were as follows: TR/TE = 160/0.35 ms, FA = 90°, spatial resolution = 4×4×4 mm^3, TA = 10 min 40 s. The parameters for

^{35}Cl MRI: TR/TE = 40/0.6 ms, FA = 90°, spatial resolution = 12×12×12 mm^3, TA = 16 min 40 s. 3T ^{1}H MR images were used as a reference. The muscular TSC was higher in patients with Cav1.1-R1239H (35.3±9.2 mM, P<0.001), Cav1.1-R528H (33.0±3.9 mM, P<0.001) mutations and ATS (24.3±0.8 mM, P = 0.035) than in controls (19.9±1.9 mM). The muscular ^{35}Cl SI was higher in patients with Cav1.1-R1239H (25.3±8.5 mM, P<0.001) and Cav1.1-R528H (22.9±3.6 mM, P<0.001) than in controls (12.2±1.6 mM) but was not higher in patients with ATS (14.3±1.9, P = 0.517). When compared with controls, patients with Cav1.1-R1239H and Cav1.1-R528H showed increased muscular edema (P<0.001 and P = 0.003, respectively) and muscle fat fraction (P<0.001 and P = 0.017, respectively). The study demonstrated that the changes of Na^+ and Cl^- homeostasis were most pronounced in the patients with Cav1.1-R1239H, with up to daily paralytic episodes. The authors of [75] believe that 7T ^{23}Na and ^{35}Cl MRI can be used to monitor myocellular ion homeostasis in clinically feasible acquisition time and may help in testing for pathogenesis, estimating prognosis, and monitoring treatment in periodic paralyses.

Myotonic dystrophy

In [76], 7 patients with myotonic dystrophy (MD) and 11 healthy volunteers were examined. ^{23}Na MR spectra were measured for calf muscles at 1.91 T field using the ^{23}Na RF head coil and the TQF method with parameters: 48-step phase cycle, 90°-pulse of 400 μs duration, NS = 336, line broadening = 10 Hz, TR = 400 ms, the evolution time of the triple quantum transition t_1 = 0.5 ms. Total sodium levels were obtained by measuring the ratio of signals from the ^{23}Na nuclei and water protons using the ^{23}Na/^{1}H surface RF coil. The water signal was used as an internal concentration standard in order to take into account the different sizes of the subjects' legs. The authors gave a range of values of Na^+/H_2O (0.5–1.3) and $T_{2,fast}$ (1.1–2.3 ms) for the group of patients and mean values for healthy volunteers (Na^+/H_2O = 0.5±0.05, $T_{2,fast}$ = 1.2±0.2 ms). Parameters Na^+/H_2O and $T_{2,fast}$ in the group of patients correlated with the stage of the disease (r^2=0.88 and r^2=0.77, respectively) and had a tendency to increase with progression of the disease. Time $T_{2,slow}$ was not sensitive to pathology, as it follows from the absence of a statistically significant difference between groups of patients and healthy volunteers. The authors note that the product of two independently measured parameters, Na^+/H_2O and $T_{2,fast}$, showed the better correlation with the stage of the disease (r^2 = 0.9). In addition, these parameters positively correlated with each other (r^2 = 0.75). In the opinion of the authors, the increase of Na^+/H_2O and $T_{2,fast}$ with increasing severity of the disease can be associated with both an expansion of the extracellular fluid volume and an increase in the intracellular sodium concentration. Myotonic dystrophy is characterized by infiltration of fatty and collagenous connective tissue. The latter is an extracellular tissue with a high Na^+ content. The growth of $T_{2,fast}$ can also be caused, according

to the authors, by a decrease of the ordering in the system at the cellular level, caused by the destruction of cell membranes.

Duchenne muscular dystrophy

In [77], 11 patients with Duchenne muscular dystrophy (DMD) and 16 healthy volunteers (controls) were examined with 3T ^{23}Na and ^{1}H MRI. The MR studies were performed on both calves using ^{23}Na/^{1}H birdcage coil. T_1-weighted turbo spin-echo (T_1W TSE) and short-tau IR (STIR) methods were applied for ^{1}H MRI. To obtain ^{23}Na MR images, two pulse sequences based on the DA 3D RPR sequence were performed: spin-density weighted ^{23}Na MRI and ^{23}Na IR-MRI. The former one was applied with the following parameters: TR/TE = 100/0.3 ms, FA = 90°, voxel size = 5×5×5 mm^3, TA=8 min 20 s. The parameters for ^{23}Na IR-MRI were: TR/TE = 124/0.3 ms, TI = 34 ms, voxel size = 6×6×6 mm^3, TA = 10 min 20 s. The normalized muscular ^{23}Na SI as assessed by the IR sequence was higher for patients with DMD than for controls (P<0.001). TSC was measured to be 38.4±6.8 mM in patients with DMD and 25.4±2.1 mM in controls. Muscular edema-like changes were detected in all patients with DMD, and the SI on STIR images was higher in patients (14.83±3.57) compared with SI in controls (6.92±0.65, P<0.001). T_1W TSE images yielded the increased level of muscular fat content in patients with DMD (0.49±0.09) relative to controls (0.39±0.01, P<0.001). The authors of [77] state that the results obtained confirm the assumption that Na^+ overload leads to muscle weakness and degeneration, similarly to patients with hypoPP in whom both increased myoplasmic Na^+ concentration and muscular edema have been observed by ^{1}H STIR MRI and ^{23}Na MRI [78]. The authors also consider that the edema-like changes in DMD patients may be caused by the intracellular Na^+ accumulation. The findings analogous to ones presented in [77] were obtained in [79] where it was shown that both muscular edema-like changes and Na^+ overload in patients with DMD persisted at follow-up. Summing up the aforementioned regarding the DMD and hypoPP, it can be assumed that the muscle edema might be mainly osmotic and intracellular.

Intervertebral disc

In [80], ^{23}Na MRI of the spine in a healthy volunteer was performed. The diagnostics was carried out at 4 T field using the transceiver ^{23}Na surface RF coil. ^{23}Na MR images were obtained using a modified 3D GRE pulse sequence with parameters: nonselective rectangular RF pulse of 400 μs duration, TR/TE = 30/1.1 ms, ST = 12 mm, MTX = 128×64×16, pixel size = 2.5×5.0 mm^2, NS = 20, TA ≈ 10 min. The ^{23}Na signal from CSF was used as an internal concentration standard, with TSC in CSF set to 140 mM. After correction for effects from the surface coil, the TSC in the intervertebral disc was determined to be 335 mM. Negatively charged glycosaminoglycans

forming the intervertebral disc attract sodium ions. Therefore TSC in intervertebral discs is directly proportional to the fixed charge density (FCD). Based on the value of TSC found, the FCD was calculated to be 0.28 mEq/g.

The aim of the study [81] was to determine the ^{23}Na MR signal value in intervertebral discs (IVD) at the level of the lumbar spine. The sample consisted of 55 healthy volunteers and 12 patients with low back pain. The correlation analysis was made for the ^{23}Na signal value and the Pfirrmann score [82]. ^{23}Na MR images were obtained at 3 T field using the 8-channel ^{23}Na RF heart coil and the DA 3D RPR pulse sequence with parameters: TR/TE = 120/0.55 ms, FA = 85°, 8000 projections, spatial resolution = 5×5×5 mm^3, FOV = 320×320×320 mm^3, TA = 16 min. In the group of healthy volunteers, the average ^{23}Na signal was smaller ($P<0.001$) in IVD with scores of 4 (0.89±0.20) and 5 (0.85±0.40) on the Pfirrmann scale than in IVD with scores of 1–3 (1.44±0.20, 1.40±0.10, 1.32±0.10). In the group of patients, the ^{23}Na signal was less ($P = 0.006$) in IVD with scores of 4 (1.00±0.40) and 5 (0.84±0.40) than in IVD with score of 2 (1.43±0.30). Intergroup differences for ^{23}Na signal in IVD with the same scores on the Pfirrmann scale were not found ($0.47<P<0.97$). In the group of healthy volunteers, the average ^{23}Na signal in IVD in women (1.46) was higher than in men (1.29), whereas the Pfirrmann scores on average did not differ (2.30 and 2.24, $P = 0.424$). In the group of patients, there was no difference in the ^{23}Na signal between men and women (1.28 in men, 1.20 in women, $P = 0.464$), but differences in Pfirrmann scores (3.36 in men, 2.56 in women, $P = 0.0002$) were found. This study shows the possibility of differentiation between non-degenerative (scores 1-3 on the Pfirrmann scale) and degenerative (scores 4 and 5) changes in IVD.

Cartilage and tendon

An excellent review regarding ^{23}Na MRI of cartilage as a potential biomarker for the evaluation of cartilage repair tissue quality and for the assessment of osteoarthritis is provided in [83]. Below are some works demonstrating advances in ^{23}Na MRI of cartilage and tendon.

The results of ^{23}Na MRI of cartilage in 6 healthy volunteers are presented in [84]. The studies were carried out at 3 and 7 T fields using the transceiver quadrature birdcage ^{23}Na RF knee coils. Two methods of obtaining ^{23}Na MR images were used: “3D radial projection reconstruction” (3D RPR) [85] and “IR wide-band uniform rate and smooth truncation” (IR WURST) [86]. The authors used the following parameters for data acquisition: TE = 0.15 ms, FA = 90°, TR = 80 ms (for 3 T), TR = 100 ms (7 T, 3D RPR), TR = 140 ms (7 T, IR WURST), TI = 22 ms (3 T, IR WURST), TI = 24 ms (7 T, IR WURST), TA = 17–25 min. As the areas of interest, the patella, femoral-tibial medial, femoral-tibial lateral and medial posterior femoral condyles were selected. The following TSC values were obtained: 171±21 mM (3 T, 3D RPR), 252±29 mM (3 T, IR WURST), 177±17

mM (7 T, 3D RPR), 278±41 mM (7 T, IR WURST). The 3D RPR method led to an underestimation of TSC because of the partial volume effect that resulted from the absence of synovial fluid suppression in this scheme.

The 3D RPR and IR WURST methods mentioned above were used in [87] in the study of patients with osteoarthritis. The sample consisted of 28 patients and 19 healthy volunteers (control group). The cartilage of the knee joint was chosen as an object of research. ^{23}Na MRI was performed at 7 T field using two RF coils. The first was a ^{23}Na birdcage knee coil. The second was a ^{23}Na/^{1}H transceiver knee coil (4-channel ^{1}H block and 8-channel ^{23}Na block). Six patients and eight healthy volunteers were diagnosed with the first coil, the rest – with the second coil. The following parameters were used for both pulse sequences: TE = 0.4 ms, FA = 90°, isotropic FOV = 200 mm, isotropic spatial resolution = 3.3 mm, 104 projections. TR was taken 100 ms for 3D RPR and 140 ms for IR WURST. The IR WURST method was additionally characterized by parameters: the duration of the adiabatic (WURST) pulse = 10 ms, its amplitude = 240 Hz, TI = 24 ms. The TSC values in the control group determined by the 3D RPR method were in the range of 180–210 mM, and in the group of patients – in the range of 170–190 mM. The mean TSC values were 192±42 mM for the control group and 174±46 mM for the group of patients. The IR WURST method gave the following results: TSC = 220–270 mM for the control group, TSC = 170–200 mM for the group of patients. The mean values for this case are not given in the paper.

The study of changes in TSC in the cartilage tissue as a result of trauma was the problem in the work [88]. The subjects of the study were 9 patients with patella dislocation. For the comparative analysis, a control group of 9 healthy volunteers was recruited. ^{23}Na MRI was performed at 7 T field using the 15-channel ^{23}Na RF transceiver RF knee coil. Morphological assessment of the state of the knee cartilage was carried out using the ^{1}H MRI method. ^{23}Na MR images (Fig. 8) were obtained using the 3D GRE pulse sequence with the parameters: TR/TE = 17.0/8.34 ms, FOV = 190×190 mm^2, 32 slices, MTX = 64×128, spatial resolution = 1.48×1.48×3.0 mm^3, BW = 80 Hz/pixel, NS = 13, FA = 50°, TA ≈ 32 min. The mean ^{23}Na SNR for cartilage in the group of patients (13.4±2.5) was less than in the control group (14.6±3.7), but no statistically significant difference was found. The negative correlation was found between the age and the global ^{23}Na SNR for cartilage in the medial facet of the diagnosed subjects ($r = –0.512$, $P = 0.03$), and between the ^{23}Na SNR and the severity of cartilage lesion ($r = –0.415$, $P<0.001$). The detection of cartilage tissue damage with ^{23}Na MRI will allow for timely surgical intervention that will prevent complications from knee joint damage.

The paper [89] is devoted to the study of biochemical changes in cartilage tissue and tendons in type 1 diabetes mellitus. The study involved 8 patients and 9 healthy volunteers (control group). The methods of diagnosis were 7T ^{1}H and ^{23}Na MRI with use of the 28-channel ^{1}H and the 15-

channel ^{23}Na RF knee coils. ^{23}Na MR images were obtained by the 3D vTE-GRE method with parameters: TR/TE = 12/1.6 ms, FA = 50°, BW = 80 Hz/pixel, spatial resolution = 1.5×1.4×3 mm^3, 40 slices, TA ≈ 28 min. ^{23}Na T_2 maps were also acquired using the double echo steady-state free precession (DESS) technique [90] with parameters: TR/TE$_1$/TE$_2$ = 8.46/4.23/12.69 ms, FOV = 140×140 mm^2, MTX = 320×320, voxel size = 0.44×0.44×3.00 mm^3, BW = 211 Hz/pixel, 32 slices, TA ≈ 2 min. In the group of patients, the ^{23}Na signal values were 76.47±15.94, 133.02±16.02 and 138.96±15.6 for the tendon of the patella, femoral cartilage of the medial and lateral condyle, respectively, while in the control group – 61.19±8.65, 156.40±18.23 and 172.6±22.3, respectively. The ^{23}Na signal values are indicated in arbitrary units. Comparative intergroup analysis gave statistically significant differences: P = 0.025, 0.014 and 0.003 for the patellar tendon, femoral cartilage medial and lateral condyle, respectively. No significantly different values were found in ^{23}Na T_2 maps in the medial (P = 0.623) and in the lateral condyle (P = 0.499) in patients. On the ^{1}H MR morphological images, cartilage in the non-weight-bearing area and the patellar tendon was intact in all patients. The authors believe that the changes of the ^{23}Na signal level detected in the cartilage tissue and tendon in patients with type 1 diabetes mellitus are a consequence of a change in the number of glycosaminoglycans caused by an increase in the production of final glycation products.

In [91], the authors set the problem of comparing glycosaminoglycan chemical exchange saturation transfer (gagCEST) imaging method [92] which enables sampling of the water signal as a function of the presaturation offset (z-spectrum) at 13 points in clinically acceptable imaging times, with ^{23}Na MRI in 12 patients after cartilage repair surgery. The MR studies were accomplished at 7 T field. The 28-channel knee coil and modified 3D GRE pulse sequence were used for gagCEST MRI, the acquisition parameters were as follows: TR/TE = 7.3/3.2 ms, FOV=146×180×84 mm^3, voxel size = 0.7×0.7×3 mm^3, TA = 14 min 34 s. ^{23}Na MRI was performed with the circularly polarized knee coil and modified 3D GRE, the acquisition parameters were as follows: TR/TE = 10/3.77 ms, FOV = 199×199×108 mm^3, voxel size = 3.10×1.55×3 mm^3, TA = 30 min 45 s. The median of asymmetries in gagCEST z-spectra summed over all offsets from 0 to 1.3 ppm was 7.99% in native cartilage and 5.13% in repair tissue. Signal ratios from native cartilage to repair tissue showed a strong correlation (r = 0.701; 95% confidence interval: 0.21, 0.91) between gagCEST and sodium values. The sodium SNR of native cartilage was higher (SNR=16.65, P<0.001) compared with that in repair tissue (SNR=11.47).

Skin

The possibility of quantitative *in vivo* determination of sodium concentration in the skin using the two-channel transceiver surface RF coil tuned to the Larmor frequency of sodium nuclei *f*=78.5

MHz (7 T field) was demonstrated in [93]. 17 healthy volunteers participated in this study. The ^{23}Na surface RF coil was placed inside the ^{1}H birdcage RF coil, which was used to obtain anatomical reference images. ^{23}Na MRI was performed using the 2D GRE pulse sequence with the following parameters: TR/TE = 135/2.27 ms, exciting gaussian pulse of 400 μs duration, FA=90°, BW = 280 Hz/pixel, FOV = 128×128 mm^2, MTX = 142×142, voxel size = 0.9×0.9×30 mm^3, NS = 32, TA ≈ 10 min. The content of sodium ions in the skin of a 25-year-old man was 41±2 mM, while in a 67-year-old male it was 1.4 times higher (57±3 mM). The linear relationship was found between TSC in the skin and age (r = 0.78), with a slope of 0.34±0.07 mM/year.

In the work [72] considered above, the growth of TSC and tissue water in the skin with age increase in both men and women was detected, the latter being lower. The authors also note an increased value of TSC in the skin in women with resistant hypertension compared with the control group.

The authors of [94] measured TSC in fibrous skin on the dorsal side of the forearm in 12 patients with systemic sclerosis. The control group consisted of 21 healthy volunteers. ^{23}Na MRI was performed at 3 T field using the ^{23}Na volume RF coil and the 2D FLASH pulse sequence with parameters: TR/TE = 100/2.07 ms, FA = 90°, NS = 128, spatial resolution = 3×3×30 mm^3, TA = 13.7 min. Representative ^{23}Na MR images are shown in Fig. 9. The authors also determined the tissue water content by the ^{1}H MRI method. TSC in the fibrotic skin of patients (27.2±5.6 mM) was higher (P<0.01) than skin TSC in the control group (21.4±5.3 mM). There were no statistically significant differences in the water content (0.19±0.06 for fibrous skin, 0.17±0.06 for healthy skin, P = 0.36), what indicates that the increase of TSC in fibrous skin is not associated with edema formation. To carry out the intragroup comparative analysis for the group of patients, the skin on the dorsal side of the calf was selected as the control. The authors found out that the TSC (26.2±4.8 mM) in the injured skin in the forearm region was higher (P<0.01) than in the control area of the skin (19.2±3.4 mM). TSC in the non-fibrous skin of patients (19.2±3.4 mM) did not differ (P = 0.16) from TSC in the skin of healthy volunteers (17.4±3.0 mM). Like in cartilage tissue, glycosaminoglycans are bound to Na^+ ions. Therefore the registration of the elevated sodium content indicates an increase in the number of glycosaminoglycans – extracellular matrix molecules. In systemic sclerosis, fibroblasts secrete a large number of glycosaminoglycans which, accumulating, can stimulate skin fibrosis.

Whole body screening

The authors of [95] conducted ^{23}Na whole body MRI for one healthy volunteer at 3 T field. To acquire ^{23}Na MR images, the volume ^{23}Na quadrature birdcage RF resonator capable of operating

both in the transceive mode and in the only transmit mode was used. In the latter case, the surface ^{23}Na RF coil operating in the only receive mode was used to receive the RF signal. The DA 3D RPR pulse sequence was applied with the following parameters: TR/TE = 49/0.5 ms, isotropic spatial resolution = 6 mm, rectangular excitation pulse of 1 ms duration, FA = 60°, BW = 60 Hz/pixel, TA = 10 min. Scanning was carried out for 5 segments of the human body: head and shoulders, upper abdomen, lower abdomen, knees and hips, lower legs and feet. The SNR maps of the data of 5 segments in the axial, coronal and sagittal planes were constructed. The composite image of the whole human body was built. The possible applications of ^{23}Na whole body MR imaging include, for example, the detection and evaluation of malignancy of cancer with metastases, as well as monitoring the response to chemotherapy.

Discussion

^{23}Na nucleus is the 2nd most abundant NMR-active nucleus in living organism after hydrogen and it plays vital role in maintaining homeostasis. The visualization of sodium-dependent processes in a body can be realized with ^{23}Na MRI that is a diagnostic tool being developed for several decades and having a great potential in providing additional biochemical information. Numerous preclinical and clinical research MR experiments demonstrated the ability of ^{23}Na MRI to recognize physiological changes occurring in different organs and tissues under different pathological states. Reviewing the advances of ^{23}Na MRI nowadays, we can suppose that ^{23}Na MRI studies of brain, kidneys, skeletal muscles, cartilage, tendon, skin and lungs might become the routine clinical procedures in near future. The value of ^{23}Na MRI for the diagnostics of breast, uterus and prostate tumors, and also heart diseases should be further investigated since, as we think, no reliable sodium measurements can be provided in these localizations at the moment.

Although, due to low NMR sensitivity and small *in vivo* concentrations of sodium nuclei, ^{23}Na MR images are of considerably lower SNR and quality relative to ^{1}H MR images, the hardware and software level reached to date allows to acquire ^{23}Na images with resolutions and SNR potentially suitable for performing the accurate quantitative analysis. Several quantitative measures can be derived *in vivo* and non-invasively from ^{23}Na MRI such as total tissue sodium concentration (TSC), intra- and extracellular sodium concentrations, ^{23}Na T_1 relaxation time, short and long ^{23}Na T_2 relaxation times, and also fixed charge density (FCD) and glycosaminoglycan (GAG) content. These parameters may suggest tissue state even at the early stage of disease and may serve as biomarkers of therapy induced functional changes in tissues.

^{23}Na MRI should be considered as a tool being performed in conjunction with other modalities such as ^{1}H MRI, CT and PET. These techniques used in combination provide a comprehensive data set with potentially more power to diagnose different diseases than any single measure alone.

Taking into account the progress in MRI achieved through the increase of main magnetic fields of MR scanners, the development of highly SNR-efficient UTE pulse sequences adapted for sodium imaging, improvements in gradient systems and in ^{23}Na RF coils, we believe that sodium imaging will be a key component of medical diagnostics in near future.

Conclusion

Sodium MRI is a quantitative *in vivo* method allowing to estimate cell integrity and tissue viability. Examples of clinical research application include cerebral stroke, brain and breast tumors, cardiac infarction, Alzheimer's disease, multiple sclerosis, hypertension, osteoarthritis, renal diseases. The use of ^{23}Na MRI in conjunction with other modalities such as ^{1}H MRI, CT and PET will improve the quality of diagnosis, therapy efficiency monitoring and prognosis of treatment outcomes.

References

[1] M. Burnier, Sodium in Health and Disease, Informa Healthcare USA, Inc., New York, 2008.

[2] E. Murphy, D.A. Eisner, Circ. Res. 104 (2009) 292–303.

[3] A.M. Rose, R. Valdes, Clin. Chem. 40 (1994) 1674–1685.

[4] K.S. Krane, Introductory nuclear physics, John Wiley & Sons, Inc., New York, 1988.

[5] J. Autschbach, S. Zheng, R.W. Schurko, Concepts Magn. Reson. Part A 36A(2) (2010) 84–126.

[6] R.K. Harris, E.D. Becker, S.M. Cabral de Menezes, R. Goodfellow, P. Grancer, Magn. Reson. Chem. 40(7) (2002) 489–505.

[7] C.P. Slichter, Principles of Magnetic Resonance, 3rd ed., Springer-Verlag, New York, 1990.

[8] D. Freude, Encycl. Anal. Chem. (2000) 12188–12224.

[9] P. Laszlo, Angew. Chem. Lnt. Ed. Engl. 17 (1978) 254–66.

[10] D. Burstein, NMR studies of intracellular sodium in the perfused frog heart. Massachusets Institute of Technology, 1986.

[11] A. Abragam, The principles of nuclear magnetism, Clarendon Press, Oxford, 1961.

[12] P.S. Hubbard, J. Chem. Phys. 53 (1970) 985–7.

[13] S. Engstrom, B. Jonsson, J. Magn. Reson. 50 (1982) 1–20.

[14] J. Andrasko, J Magn Reson 16 (1974) 502–4.

[15] S.C. Niesporek, S.H. Hoffmann, M.C. Berger, N. Benkhedah, A. Kujawa, P. Bachert, A.M. Nagel, Neuroimage 112 (2015) 353–363.

[16] A.M. Lu, I.C. Atkinson, T.C. Claiborne, F.C. Damen, K.R. Thulborn, Magn. Reson. Med. 63 (2010) 1583–1593.

[17] J. Lommen, S. Konstandin, P. Krämer, L.R. Schad, NMR Biomed. 29 (2016) 129–136.

[18] A.M. Nagel, R. Umathum, M.B. Rösler, M.E. Ladd, I. Litvak, P.L. Gor'kov, W.W. Brey, V.D. Schepkin, NMR Biomed. 29(6) (2016) 759–766.

[19] G. Madelin, R.R. Regatte, J Magn Reson Imaging 38(3) (2013) 511–29.

[20] K.R. Thulborn, Neuroimage 168 (2016) 250–68.

[21] S. Konstandin, A.M. Nagel, Magn Reson Mater Phy 27(1) (2014) 5–19.

[22] E.A. Mellon, D.T. Pilkinton, C.M. Clark, M.A. Elliott, W.R. Witschey 2nd, A. Borthakur, R. Reddy, Am. J. Neuroradiol. 30 (2009) 978–84.

[23] K. Reetz, S. Romanzetti, I. Dogan, C. Sass, C.J. Werner, J. Schiefer, J.B. Schulz, N.J. Shah, Neuroimage 63 (2012) 517–524.

[24] S. Romanzetti, M. Halse, J. Kaffanke, K. Zilles, B.J. Balcom, N.J. Shah, J. Magn. Reson. 179 (2006) 64–72.

[25] B.J. Balcom, R.P. Macgregor, S.D. Beyea, D.P. Green, R.L. Armstrong, T.W. Bremner, J. Magn. Reson. A 123 (1996) 131–134.

[26] M. Petracca, L. Fleysher, N. Oesingmann, M. Inglese, NMR Biomed. 29(2) (2016) 153–161.

[27] M. Inglese, G. Madelin, N. Oesingmann, J.S. Babb, W. Wu, B. Stoeckel, J. Herbert, G. Johnson, Brain 133 (2010) 847–857.

[28] W. Zaaraoui, S. Konstandin, B. Audoin, A.M. Nagel, A. Rico, I. Malikova, E. Soulier, P. Viout, S. Confort-Gouny, P.J. Cozzone, J. Pelletier, L.R. Schad, J.-P. Ranjeva, Radiology 264(3) (2012) 859–67.

[29] A.M. Nagel, F.B. Laun, M.-A. Weber, C. Matthies, W. Semmler, L.R. Schad, Magn. Reson. Med. 62 (2009) 1565–1573.

[30] M. Petracca, R.O. Vancea, L. Fleysher, L.E. Jonkman, N. Oesingmann, M. Inglese, Brain 139 (2016) 795–806.

[31] S.M. Grieve, B. Wickstead, A.M. Torres, P. Styles, S. Wimperis, P.W. Kuchel, Biophys. Chem. 73 (1998) 137–143.

[32] A.M. Torres, D.J. Philp, R. Kemp-Harper, C. Garvey, P.W. Kuchel, Magn. Reson. Chem. 43 (2005) 217–224.

[33] Y. Zhang, M. Poirer-Quinot, C.S. Springer Jr., J.A. Balschi, J. Magn. Reson. 205 (2010) 28–37.

[34] J.S. Tauskela, J.M. Dizon, J. Whang, J. Katz, J. Magn. Reson. 127 (1997) 115–127.

[35] J.M. Dizon, J.S. Tauskela, D. Wise, D. Burkhoff, P.J. Cannon, J. Katz, Magn. Reson. Med. 35 (1996) 336–345.

[36] V.D. Schepkin, I.O. Choy, T.F. Budinger, D.Y. Obayashi, S.E. Taylor, W.M. DeCampli,

S.C. Amartur, J.N. Young, Magn. Reson. Med. 39 (1998) 557–563.
[37] G. Navon, J.G. Werrmann, R. Maron, S.M. Cohen, Magn. Reson. Med. 32 (1994) 556–564.
[38] J.L. Allis, A.-M.L. Seymour, G.K. Radda, J. Magn. Reson. 93 (1991) 71–76.
[39] U. Eliav, H. Shinar, G. Navon, J. Magn. Reson. 94 (1991) 439–444.
[40] G. Jaccard, S. Wimperis, G. Bodenhausen, J. Chem. Phys. 85 (1986) 6282–6293.
[41] S. Wimperis, B. Wood, J. Magn. Reson. 95 (1991) 428–436.
[42] W.D. Rooney, C.S. Springer, NMR Biomed. 4 (1991) 227–245.
[43] W.D. Rooney, C.S. Springer, NMR Biomed 4 (1991) 209–226.
[44] G. Navon, H. Shinar, U. Eliav, S. Yoshiteru, NMR Biomed. 14 (2001) 112–132.
[45] T.B. Parrish, D.. Fieno, S.W. Fitzgerald, R.M. Judd, Magn. Reson. Med. 38 (1997) 653–661.
[46] A. Tsang, R.W. Stobbe, N. Asdaghi, M.S. Hussain, Y.A. Bhagat, C. Beaulieu, D. Emery, K.S. Butcher, J. Magn. Reson. Imaging 33 (2011) 41–47.
[47] R. Stobbe, C. Beaulieu, Magn. Reson. Med. 59 (2008) 345–55.
[48] P.M. Heiler, F.L. Langhauser, F. Wetterling, S. Ansar, S. Grudzenski, S. Konstandin, M. Fatar, S. Meairs, L.R. Schad, J. Magn. Reson. Imaging 34 (2011) 935–940.
[49] R. Ouwerkerk, K.B. Bleich, J.S. Gillen, M.G. Pomper, P.A. Bottomley, Radiology 227 (2003) 529–537.
[50] F.E. Boada, J.S. Gillen, G.X. Shen, S.Y. Chang, K.R. Thulborn, Magn. Reson. Med. 37 (1997) 706–715.
[51] F.E. Boada, G.X. Shen, S.Y. Chang, K.R. Thulborn, Magn. Reson. Med. 38 (1997) 1022–1028.
[52] D.P. Fiege, S. Romanzetti, C. Mirkes, D. Brenner, N.J. Shah, Magn. Reson. Med. 69 (2013) 1691–1696.
[53] R.P. Kline, E.X. Wu, D.P. Petrylak, M. Szabolcs, P.O. Alderson, M.L. Weisfeldt, P. Cannon, J. Katz, Clin. Cancer Res. 6 (2000) 2146–2156.
[54] A.M. Nagel, M. Bock, C. Hartmann, L. Gerigk, J.O. Neumann, M.A. Weber, M. Bendszus, A. Radbruch, W. Wick, H.P. Schlemmer, W. Semmler, A. Biller, Invest Radiol 46(9) (2011) 539–47.
[55] A. Biller, S. Badde, A. Nagel, J.O. Neumann, W. Wick, A. Hertenstein, M. Bendszus, F. Sahm, N. Benkhedah, J. Kleesiek, AJNR Am J Neuroradiol 37 (2016) 66–73.
[56] C.M. Laymon, M.J. Oborski, V.K. Lee, D.K. Davis, E.C. Wiener, F.S. Lieberman, F.E. Boada, J.M. Mountz, Magn Reson Imaging 30(9) (2012) 1268–78.
[57] A.M. Nagel, F. Lehmann-Horn, M.A. Weber, K. Jurkat-Rott, M.B. Wolf, A. Radbruch, R. Umathum, W. Semmler, Radiology 271(2) (2014) 585–95.

[58] R. Ouwerkerk, M.A. Jacobs, K.J. Macura, A.C. Wolff, V. Stearns, S.D. Mezban, N.F. Khouri, D.A. Bluemke, P.A. Bottomley, Breast Cancer Res. Treat. 106 (2007) 151–160.

[59] M. Danisch, R. Kalayciyan, F. Wetterling, L.R. Schad, Z. Med. Phys. 24 (2014) 65–72.

[60] T. Henzler, S. Konstandin, G. Schmid-Bindert, P. Apfaltrer, S. Haneder, F. Wenz, L. Schad, C. Manegold, S.O. Schoenberg, C. Fink, Fortschr Röntgenstr 184 (2012) 340–344.

[61] R. Ouwerkerk, P.A. Bottomley, M. Solaiyappan, A.E. Spooner, G.F. Tomaselli, K.C. Wu, R.G. Weiss, Radiology 248(1) (2008) 88–96.

[62] A. Graessl, A. Ruehle, H. Waiczies, A. Resetar, S.H. Hoffmann, J. Rieger, F. Wetterling, L. Winter, A.M. Nagel, T. Niendorf, NMR Biomed. 28 (2015) 967–975.

[63] F.G. Zöllner, S. Konstandin, J. Lommen, J. Budjan, S.O. Schoenberg, L.R. Schad, S. Haneder, NMR Biomed. 29(2) (2016) 197–205.

[64] N. Maril, Y. Rosen, G.H. Reynolds, A. Ivanishev, L. Ngo, R.E. Lenkinski, Magn. Reson. Med. 56 (2006) 1229–1234.

[65] S. Haneder, V. Juras, H.J. Michaely, X. Deligianni, O. Bieri, S.O. Schoenberg, S. Trattnig, Š. Zbýň, Eur Radiol 24 (2014) 494–501.

[66] S. Haneder, H.J. Michaely, S. Konstandin, L.R. Schad, J.N. Morelli, B.K. Krämer, S.O. Schoenberg, A. Lammert, Magn Reson Mater Phy 27 (2014) 47–52.

[67] J. Budjan, U. Benck, A. Lammert, M.M. Ong, M. Mircheva, S. Diehl, S. Konstandin, L.R. Schad, B.K. Krämer, S.O. Schoenberg, S. Haneder, In Vivo (Brooklyn). 30 (2016) 657–62.

[68] D. Hausmann, S. Konstandin, F. Wetterling, S. Haneder, A.M. Nagel, D.J. Dinter, S.O. Schönberg, F.G. Zöllner, L.R. Schad, Invest Radiol 47(12) (2012) 677–82.

[69] A. Farag, J.C. Peterson, T. Szekeres, G. Bauman, J. Chin, C. Romagnoli, R. Bartha, T.J. Scholl, J. Magn. Reson. Imaging 42 (2015) 436–445.

[70] M.A. Jacobs, R. Ouwerkerk, I. Kamel, P.A. Bottomley, D.A. Bluemke, H.S. Kim, J. Magn. Reson. Imaging 29 (2009) 649–56.

[71] G. Chang, L. Wang, M.E. Schweitzer, R.R. Regatte, Eur. Radiol. 20 (2010) 2039–46.

[72] C. Kopp, P. Linz, A. Dahlmann, M. Hammon, J. Jantsch, D.N. Müller, R.E. Schmieder, A. Cavallaro, K.U. Eckardt, M. Uder, F.C. Luft, J. Titze, Hypertension 61 (2013) 635–40.

[73] A.M. Nagel, E. Amarteifio, F. Lehmann-Horn, K. Jurkat-Rott, W. Semmler, L.R. Schad, M.A. Weber, Invest Radiol 46(12) (2011) 759–66.

[74] E. Amarteifio, A.M. Nagel, M.A. Weber, K. Jurkat-Rott, F. Lehmann-Horn, Radiology 264(1) (2012) 154–63.

[75] M.A. Weber, A.M. Nagel, A.M. Marschar, P. Glemser, K. Jurkat-Rott, M.B. Wolf, M.E. Ladd, H.P. Schlemmer, H.U. Kauczor, F. Lehmann-Horn, Radiology 280(3) (2016) 848–59.

[76] T. Kushnir, T. Knubovets, Y. Itzchak, U. Eliav, M. Sadeh, L. Rapoport, E. Kott, G. Navon, Magn. Reson. Med. 37 (1997) 192–6.

[77] M.A. Weber, A.M. Nagel, K. Jurkat-Rott, F. Lehmann-Horn, Neurology 77(23) (2011) 2017–24.

[78] K. Jurkat-Rott, M.A. Weber, M. Fauler, X.H. Guo, B.D. Holzherr, A. Paczulla, N. Nordsborg, W. Joechle, F. Lehmann-Horn, Proc Natl Acad Sci USA 106 (2009) 4036–4041.

[79] M.A. Weber, A.M. Nagel, M.B. Wolf, K. Jurkat-Rott, H.U. Kauczor, W. Semmler, F. Lehmann-Horn, J Neurol 259(11) (2012) 2385–92.

[80] E.K. Insko, D.B. Clayton, M.A. Elliott, Acad Radiol 9 (2002) 800–4.

[81] S. Haneder, M.M.L. Ong, J.M. Budjan, R. Schmidt, S. Konstandin, J.N. Morelli, L.R. Schad, S.O. Schoenberg, U.H. Kerl, Spine J. 14 (2014) 1343–50.

[82] C.W. Pfirrmann, A. Metzdorf, M. Zanetti, J. Hodler, N. Boos, Spine (Phila Pa 1976) 26(17) (2001) 1873–8.

[83] S. Zbýn, V. Mlynárik, V. Juras, P. Szomolanyi, S. Trattnig, NMR Biomed. 29(2) (2016) 206–15.

[84] G. Madelin, J.S. Babb, D. Xia, G. Chang, A. Jerschow, R.R. Regatte, Magn. Reson. Med. 68 (2012) 841–849.

[85] S. Nielles-Vallespin, M.A. Weber, M. Bock, A. Bongers, P. Speier, S.E. Combs, J. Wöhrle, F. Lehmann-Horn, M. Essig, L.R. Schad, Magn. Reson. Med. 57 (2007) 74–81.

[86] E. Kupce, R. Freeman, J Magn Reson A 115 (1995) 273–276.

[87] G. Madelin, J. Babb, D. Xia, G. Chang, S. Krasnokutsky, S.B. Abramson, A. Jerschow, R.R. Regatte, Radiology 268 (2013) 481–491.

[88] H.K. Widhalm, S. Apprich, G. Welsch, S. Zbyn, P. Sadoghi, G. Vekszler, M. Hamboeck, M. Weber, S. Hajdu, S. Trattnig, Knee Surg Sport. Traumatol Arthrosc 24 (2016) 1601–9.

[89] W. Marik, S.F. Nemec, Š. Zbýň, M. Zalaudek, B. Ludvik, G. Riegler, M. Karner, S. Trattnig, Invest. Radiol. 51(4) (2016) 266–72.

[90] H. Bruder, H. Fischer, R. Graumann, M. Deimling, Magn Res Med 7(1) (1988) 35–42.

[91] B. Schmitt, S. Zbýn, D. Stelzeneder, V. Jellus, D. Paul, L. Lauer, P. Bachert, S. Trattnig, Radiology 260(1) (2011) 257–64.

[92] W. Ling, R.R. Regatte, G. Navon, A. Jerschow, Proc Natl Acad Sci USA 105(7) (2008) 2266–2270.

[93] P. Linz, D. Santoro, W. Renz, J. Rieger, A. Ruehle, J. Ruff, M. Deimling, N. Rakova, D.N. Muller, F.C. Luft, J. Titze, T. Niendorf, NMR Biomed. 28 (2015) 54–62.

[94] C. Kopp, C. Beyer, P. Linz, A. Dahlmann, M. Hammon, J. Jantsch, P. Neubert, D. Rosenhauer, D.N. Muller, A. Cavallaro, K.-U. Eckardt, G. Schett, F.C. Luft, M. Uder,

J.H.W. Distler, J. Titze, Rheumatology 56(4) (2017) 556–60.

[95] F. Wetterling, D.M. Corteville, R. Kalayciyan, A. Rennings, S. Konstandin, A.M. Nagel, H. Stark, L.R. Schad, Phys. Med. Biol. 57 (2012) 4555–67.

List of figures:

Fig. 1 The charge distribution of nuclei with different spins and quadrupole moments

Fig. 2 The energy level diagram for a nucleus with spin 3/2 [10]

Fig. 3 The spectral density function for different τ_c [10]

Fig. 4 Three types of spectra occuring for nuclei with 3/2 spin: (a) $\tau_c << 1/\omega_0$, one resonance peak; (b) $\tau_c \approx 1/\omega_0$, two superimposed resonance peaks; (c) $\tau_c >> 1/\omega_0$, three different resonance peaks. The numbers reflect the relative areas of the resonance peaks [10]

Fig. 5 MRI and PET images from a patient 1 with deep right-sided posterior frontoparietal glioblastoma multiforme (GBM). (A) ^{1}H anatomical MR image (MPRAGE); (B) contrast-enhanced ^{1}H T_1 MRI; (C) ^{1}H FLAIR MRI; (D) ^{23}Na MRI; (E) F-18 FLT PET tracer distribution volume derived from a 68-min dynamic PET series; (F) an F-18 FLT PET image acquired over the period from 0 to 2 min post tracer injection (normalized to average activity in the carotid artery) showing early tracer wash-in. Reproduced with permission from Ref. [56]

Fig. 6 MRI, CT and PET images from a patient with an adenocarcinoma of the left upper lung lobe. Contrast-enhanced CT (A) shows central necrosis (asterisk). On F-18 FDG PET-CT ((B) fused PET-CT, (C) PET)), the viable tumor shows strong FDG accumulation (SUV_{max} = 43), while the necrotic tumor shows no FDG accumulation. Also the infero-lateral margin of the tumor shows no FDG accumulation (arrow), which demonstrates that this part of the tumor is less viable. Similarly, ^{23}Na MRI ((D) T_1 weighted ^{1}H GRE MRI, (E) fused ^{23}Na MRI, (F) ^{23}Na MRI) indicates that the infero-lateral margin of the tumor is less viable and has a low SI, while the viable tumor margin has a high SI. In addition, the central tumor necrosis also has high signal intensity. Reproduced with permission from Ref. [60]

Fig. 7 Color-encoded ^{23}Na-distribution maps of the left kidney in a patient with central diabetes insipidus before (A) and after (B) intranasal administration of 20 μg desmopressin (DDAVP). Reproduced with permission from Ref. [66]

Fig. 8 Axial 2D proton-density weighted TSE fat-suppressed MR image (*left*) from a patient with patella dislocation and corresponding sodium MR image (*right*). The *yellow arrows* mark cartilage defects on the lateral facet near the intermediary zone of the patella. The *orange borders* symbolize the ROI analysis for the medial intermediary and lateral facet. Reproduced with permission from Ref. [88]

Fig. 9 ^{23}Na and ^{1}H MR images of healthy (*left*) and fibrotic skin (*right*). Calibration tubes (40, 30, 20 and 10 mM) are placed below the forearm. The arrows indicate the site of measurement. Reproduced with permission from Ref. [94]

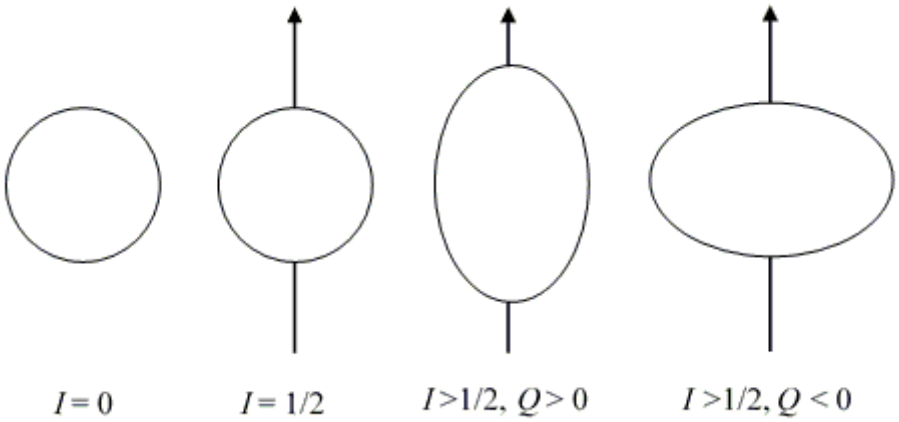
I = 0
I = 1/2
I >1/2, Q > 0
I >1/2, Q < 0

Fig. 1

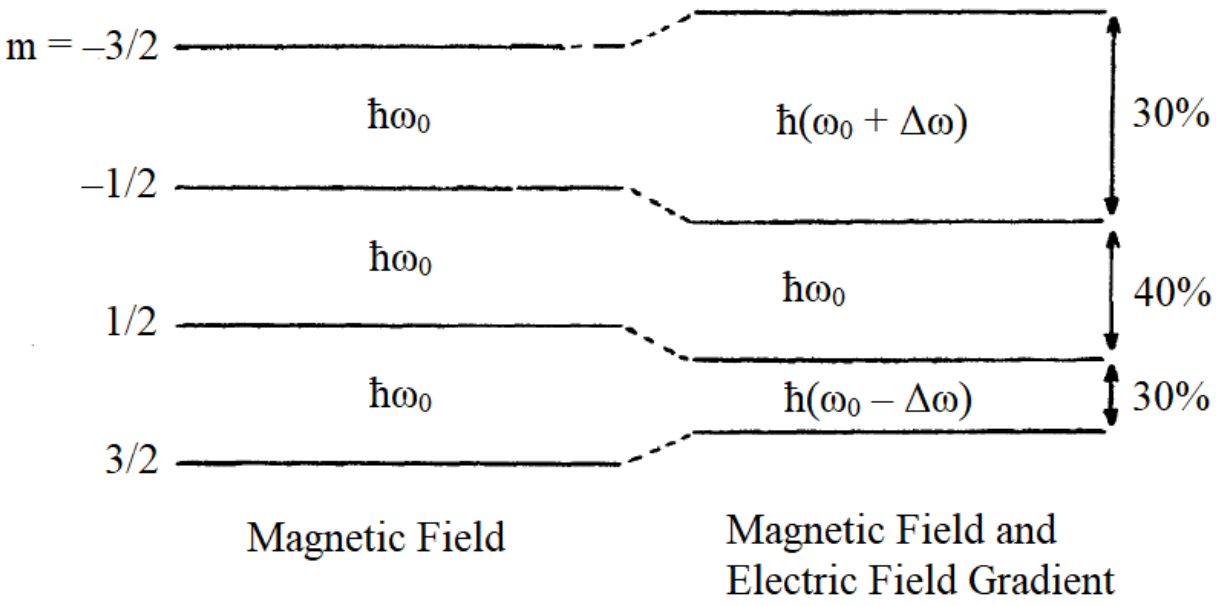
m = –3/2
–1/2
1/2
3/2
ħω0
ħω0
ħω0
ħ(ω0 + Δω)
ħω0
ħ(ω0 – Δω)
30%
40%
30%
Magnetic Field
Magnetic Field and
Electric Field Gradient

Fig. 2

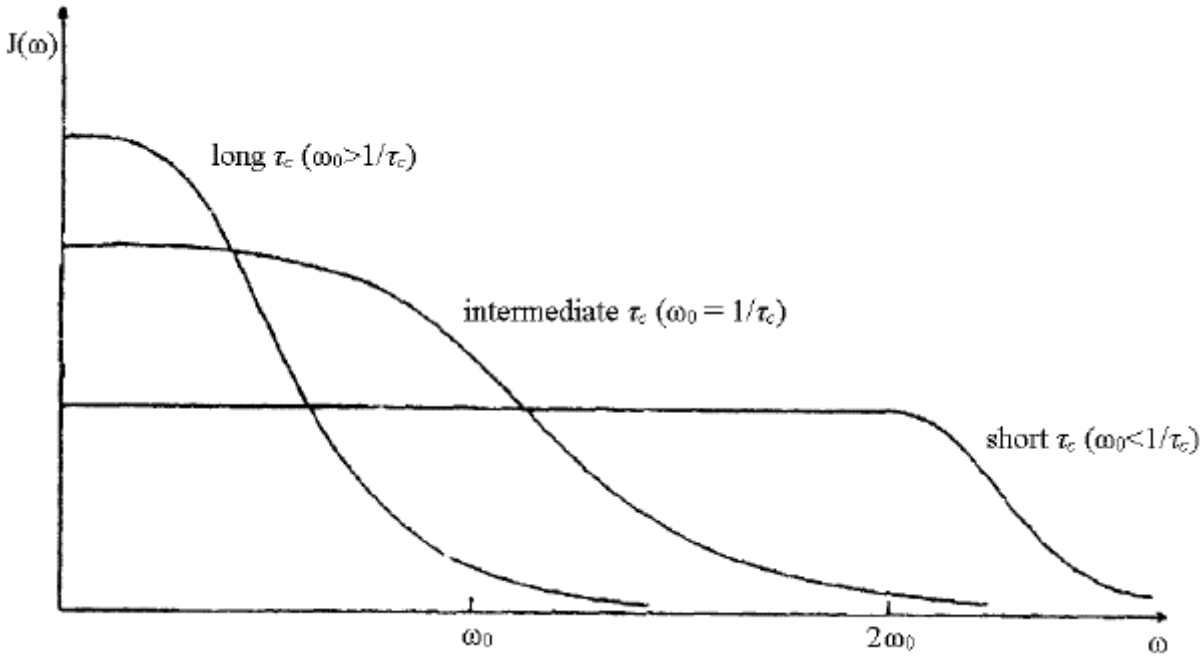
J(ω)
long τ_c ($\omega_0 > 1/\tau_c$)
intermediate τ_c ($\omega_0 = 1/\tau_c$)
short τ_c ($\omega_0 < 1/\tau_c$)
ω_0
$2\omega_0$
ω

Fig. 3

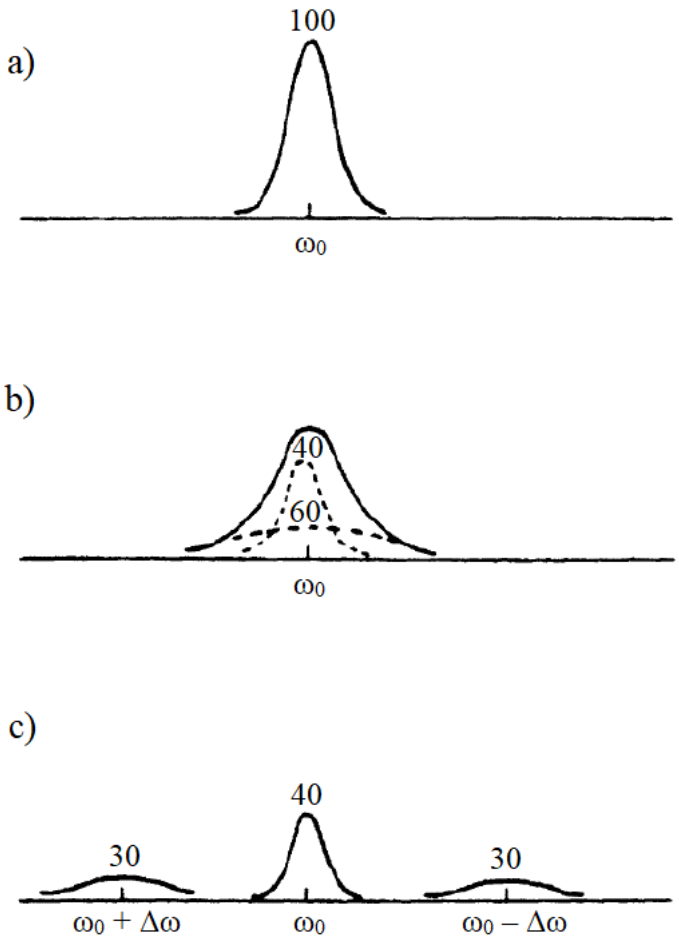
a)
100
ω_0
b)
40
60
ω_0
c)
40
30
30
$\omega_0 + \Delta\omega$
ω_0
$\omega_0 - \Delta\omega$

Fig. 4

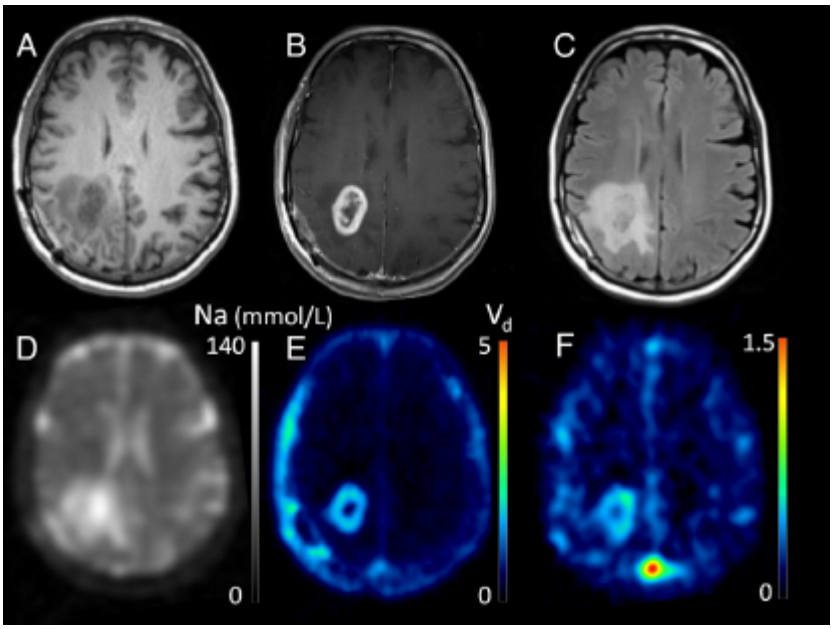

Fig. 5

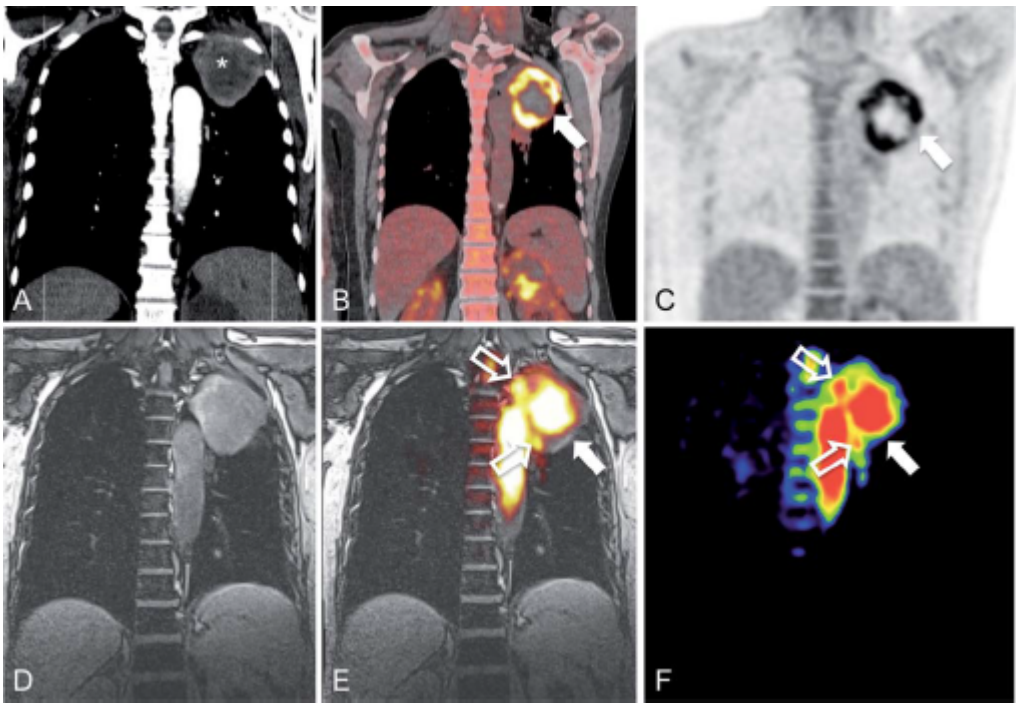

Fig. 6

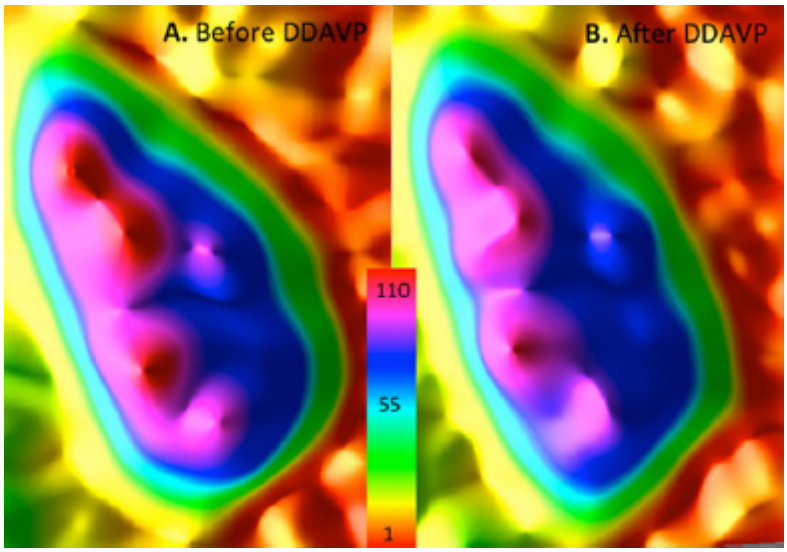
A. Before DDAVP
B. After DDAVP
110
55
1

Fig. 7

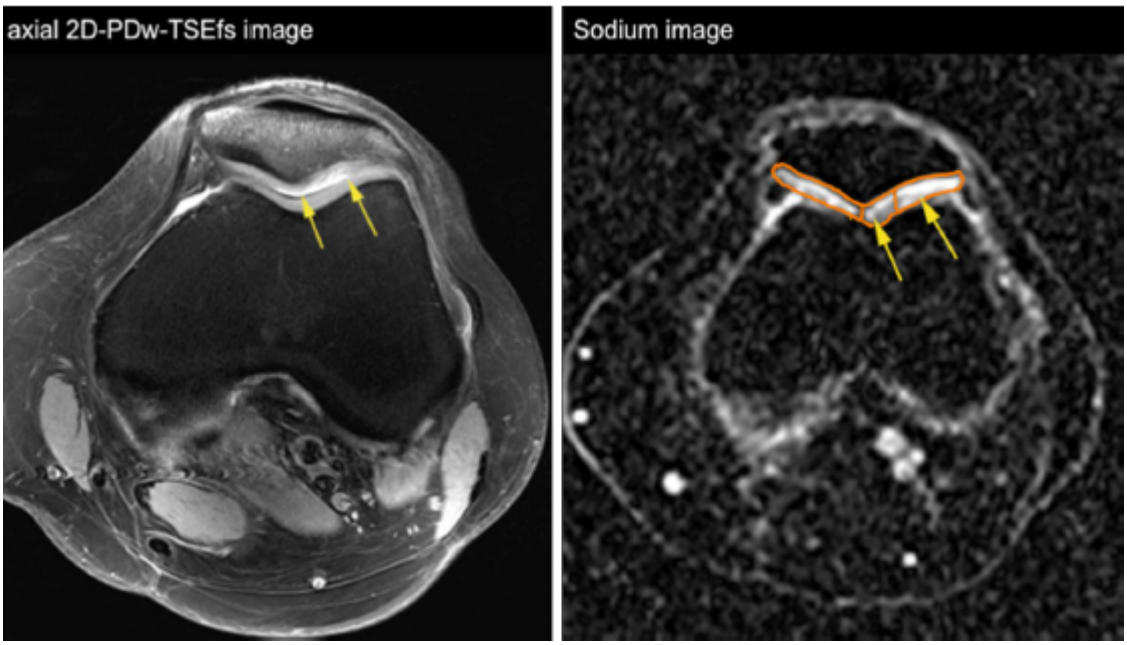
axial 2D-PDw-TSEfs image
Sodium image

Fig. 8

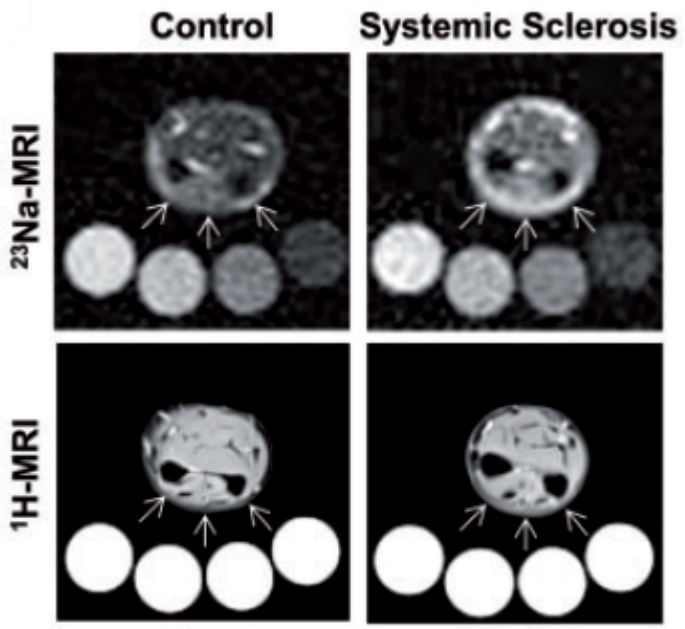

Fig. 9